

¹ Study of the multi-strange resonance $\Xi(1530)^0$ production
² with ALICE at the LHC energies

³ Jihye Song

4 Contents

5	List of Figures	4
6	List of Tables	8
7	1 The physics of relativistic heavy-ion collisions	9
8	1.1 Standard model	9
9	1.2 QCD and Quark-Gluon plasma	10
10	1.3 Heavy Ion Collisions	15
11	2 Production of resonance with strangeness	17
12	2.1 Strange quark and hyperons	17
13	2.2 Resonance production	17
14	3 Theoretical models	17
15	3.1 Thermal statistical model	17
16	3.1.1 Calculations	19
17	3.1.2 Results	19
18	3.1.3 Comparison with data	21
19	3.2 UrQMD	21
20	4 A Large Ion Collider Experiment at the LHC	22
21	4.1 The Large Hadron Collider	22
22	4.2 The ALICE project	25
23	4.2.1 ALICE detector	25
24	4.2.2 Data Acquisition (DAQ) and trigger system	35
25	4.2.3 ALICE offline software framework	37
26	5 Measurement of $\Xi(1530)^0$ production in p-Pb and Pb-Pb	39
27	5.1 $\Xi(1530)^0$ -reconstruction	39
28	5.1.1 Data sample and event selection	39
29	5.1.2 Track and topological selection	43
30	5.1.3 Particle identification	46
31	5.1.4 Signal extraction	49
32	5.2 Efficiency correction	58
33	5.3 Corrected p_T -spectra	61
34	5.4 Systematic uncertainties	63
35	5.5 $\Xi(1530)^0$ transverse momentum spectra	68

36	6 Further results and discussion	71
37	6.1 Mean transverse momentum	71
38	6.2 Particle yield ratios	75
39	6.2.1 Integrated yield ratios of excited to ground-state hadrons	75
40	6.3 Integrated yield ratios to pion	78
41	References	82

42 **List of Figures**

43	1	Standard Model families of leptons and quarks as the gauge bosons	9
44	2	Summary of measurements of β_s as a function of the respective energy scale Q. The respective degree of QCD perturbation theory used in the extraction of β_s is indicated in brackets (NLO: next-to-leading order; NNLO: next-to-next-to leading order; res. NNLO: NNLO matched with resummed next-to-leading logs; N3LO: next-to-NNLO) [1]	13
45	3	Hydrodynamic evolution of a heavy ion collision with and without the for- mation of a QGP.	16
46	4	Ratio of baryonic and mesonic resonances over their stable partner as a function of temperature.	20
47	5	Ratio of resonances over their stable partner as a function of $\sqrt(s)$	21
48	6	The CERN accelerator complex [2]	23
49	7	The ALICE detector	27
50	8	Schematic view of the ITS [3]	28
51	9	Track impact parameter resolution in the transverse plane ($r\phi$) vs p_T for charged particle	29
52	10	Schematic view of the TPC	30
53	11	Specific energy loss (dE/dx) in the TPC vs. particle momentum in Pb–Pb collisions at $\sqrt{s_{NN}} = 2.76$ TeV. The lines show the parametrisations of the expected mean energy loss.	31
54	12	Correlation between the sum and difference of signal times in V0A and V0C. Three classes of events collisions at (8.3 ns, 14.3 ns), background from Beam 1 at (-14.3 ns, -8.3 ns), and background from Beam 2 at (14.3 ns, 8.3 ns) can be clearly distinguished.	33
55	13	Distribution of the V0 amplitude (sum of V0A and V0C in top, V0A in bottom). The inset shows a magnified version of the most peripheral region. .	34
56	14	The overall architecture of the ALICE DAQ and the interface to the HLT system.	35
57	15	Schematic view of the AliRoot framework	38
58	16	Vertex-z coordinate distribution of the accepted events in p–Pb collision(Left) and in Pb–Pb collisions(Right). The red dashed line indicates vertex cut .	41
59	17	Multiplicity distribution of accepted events in p–Pb collision in percentile. The each color and labels define the four intervals in which the analysis is performed.	41
60	18	Centrality distribution of three different trigger classes.	42
61	19	Sketch of the decay modes for Ξ^{*0} and depiction of the track and topological selection criteria.	44
62	20	TPC dE/dx as function of transverse momentum for total (top) and selected first emitted π in 3σ (bottom)	46

82	21	TPC dE/dx as function of transverse momentum for total (top) and selected second emitted π in 3σ (bottom)	46
84	22	TPC dE/dx as function of transverse momentum for total (top) and selected last emitted π in 3σ (bottom)	47
86	23	TPC dE/dx as function of transverse momentum for total (top) and selected proton in 3σ (bottom)	47
88	24	TPC dE/dx as function of transverse momentum for total (top) and selected first emitted π in 3σ (bottom)	47
90	25	TPC dE/dx as function of transverse momentum for total (top) and selected second emitted π in 3σ (bottom)	48
92	26	TPC dE/dx as function of transverse momentum for total (top) and selected last emitted π in 3σ (bottom)	48
94	27	TPC dE/dx as function of transverse momentum for total (top) and selected proton in 3σ (bottom)	49
96	28	The $\Xi^\mp\pi^\pm$ invariant mass distribution (Same-event pairs) in $1.8 < p_T < 2.2 \text{ GeV}/c$ and for the multiplicity class 20-40%. The background shape, using pairs from different events (Mixed-event background), is normalised to the counts in $1.49 < M_{\Xi\pi} < 1.51 \text{ GeV}/c^2$ and $1.56 < M_{\Xi\pi} < 1.58 \text{ GeV}/c^2$	50
100	29	The $\Xi^\mp\pi^\pm$ invariant mass distribution (Same-event pairs) in $3.0 < p_T < 3.5 \text{ GeV}/c$ and for the centrality class 0-10%. The background shape, using pairs from different events (Mixed-event background), is normalised to the counts in $1.49 < M_{\Xi\pi} < 1.51 \text{ GeV}/c^2$ and $1.56 < M_{\Xi\pi} < 1.58 \text{ GeV}/c^2$	51
104	30	The invariant mass distribution after subtraction of the mixed-event background in p–Pb collisions. The solid curve represents the combined fit, while the dashed line describes the residual background.	52
108	31	The invariant mass distribution after subtraction of the mixed-event background in Pb–Pb collisions. The solid curve represents the combined fit, while the dashed line describes the residual background.	53
110	32	σ fit parameters as a function of p_T in MB in p–Pb collisions (top) and in Pb–Pb collisions (bottom).	55
112	33	$\Xi(1530)^0$ -mass obtained from fit of the Voigtian peak as a function of p_T in each multiplicity classes in p–Pb collisions (top) and the different centrality classes in Pb–Pb (bottom).	56
115	34	$\Xi(1530)^0$ -raw spectra obtained from fit of the Voigtian peak and a polynomial residual background for different multiplicities in p–Pb collisions (top) and Pb–Pb collisions (bottom). Only the statistical error is reported.	57
118	35	$\Xi(1530)^0$ -raw spectra obtained from fit of the Voigtian peak and a polynomial residual background for different multiplicities. Only the statistical error is reported.	58

121	36	Real corrected $\Xi(1530)^0$ spectrum (black) for the minimum bias with Levy fit (black curve). Also shown are the unweighted generated (blue) and reconstructed (red) $\Xi(1530)^0$ spectra.	59
122	37	Efficiency as a function of p_{T} in minimum bias events in p–Pb collisions.	60
123	38	Efficiency as a function of p_{T} in different centrality classes in Pb–Pb collisions	61
124	39	Corrected p_{T} -spectra of $\Xi(1530)^0$ in NSD and different multiplicity classes in p–Pb collisions.	62
125	40	Corrected p_{T} -spectra of $\Xi(1530)^0$ in different centrality classes in Pb–Pb collisions.	62
126	41	Summary of the contributions to the systematic uncertainty in minimum bias events in p–Pb collisions. The dashed black line is the sum in quadrature of all the contributions.	66
127	42	Systematic uncertainties for each multiplicity classes in p–Pb collisions.	66
128	43	Summary of the contributions to the systematic uncertainty in minimum bias events in Pb–Pb collisions. The dashed black line is the sum in quadrature of all the contributions.	67
129	44	Systematic uncertainties for each multiplicity classes.	67
130	45	Corrected yields as function of p_{T} in NSD events and multiplicity dependent event classes in p–Pb collision system. Statistical uncertainties are presented as bar and systematical uncertainties are plotted as boxes.	69
131	46	Corrected yields as function of p_{T} in different centrality classes in Pb–Pb collision system. Statistical uncertainties are presented as bar and systematical uncertainties are plotted as boxes.	70
132	47	Mean transverse momenta $\langle p_{\text{T}} \rangle$ of Λ , Ξ^- , $\Sigma^{*\pm}$, Ξ^{*0} and Ω^- in p–Pb collisions at $\sqrt{s_{\text{NN}}} = 5.02$ TeV as a function of mean charged-particle multiplicity density $\langle dN_{\text{ch}}/d\eta_{\text{lab}} \rangle$, measured in the pseudorapidity range $ \eta_{\text{lab}} < 0.5$. The results for Λ , Ξ^- and Ω^- are taken from [4, 5, 6]. Statistical and systematic uncertainties are represented as bars and boxes, respectively. The Ω^- and Ξ^- points in the 3rd and 4th lowest multiplicity bins are slightly displaced along the abscissa to avoid superposition with the $\Xi(1530)^0$ points.	72
133	48	Mass dependence of the mean transverse momenta of identified particles for the 0 – 20% V0A multiplicity class and with $-0.5 < y_{\text{CMS}} < 0$ in p–Pb collisions at $\sqrt{s_{\text{NN}}} = 5.02$ TeV [4, 6], and in minimum-bias pp collisions at $\sqrt{s} = 7$ TeV [7] with $ y_{\text{CMS}} < 0.5$. Additionally, D^0 and J/ψ results are plotted. The D^0 and J/ψ were measured in different rapidity ranges: $ y_{\text{CMS}} < 0.5$ [8] ($ y_{\text{CMS}} < 0.9$ [9]) for D^0 (J/ψ) in pp and $-0.96 < y_{\text{CMS}} < 0.04$ [8] ($-1.37 < y_{\text{CMS}} < 0.43$ [10]) for D^0 (J/ψ) in p–Pb. Note also that the results for D^0 and J/ψ in p–Pb collisions are for the 0–100% multiplicity class.	73

160	49	Ratio of $\Xi(1530)^0$ to Ξ^- measured in pp [7], p–Pb [4, 6] and Pb–Pb collisions as a function of $\langle dN_{ch}/d\eta_{lab} \rangle$ measured at midrapidity. Statistical uncertainties (bars) are shown as well as total systematic uncertainties (hollow boxes) and systematic uncertainties uncorrelated across multiplicity (shaded boxes). A few model predictions are also shown as lines at their appropriate abscissa.	76
161			
162			
163			
164			
165			
166	50	Ratio of ρ/π (Up), K^*/K , ϕ/K (Left bottom) and Λ^*/Λ with system size measured at mid-rapidity. Statistical uncertainties (bars) are shown as well as total systematic uncertainties (hollow boxes) and systematic uncertainties uncorrelated across multiplicity (shaded boxes). A few model predictions are also shown as lines at their appropriate abscissa.	77
167			
168			
169			
170			
171	51	Ratio of $\Xi(1530)^0$ to π^\pm , measured in pp [11] and p–Pb [7] collisions, as a function of the average charged particle density ($\langle dN_{ch}/d\eta_{lab} \rangle$) measured at mid-rapidity. Statistical uncertainties (bars) are shown as well as total systematic uncertainties (hollow boxes) and systematic uncertainties uncorrelated across multiplicity (shaded boxes). A few model predictions are also shown as lines at their appropriate abscissa.	79
172			
173			
174			
175			
176			
177	52	Particle yield ratios to pions of strange and multi-strange hadrons normalized to the values measured in pp collisions, both in pp and in p–Pb collisions. The common systematic uncertainties cancel in the double-ratio. The empty boxes represent the remaining uncorrelated uncertainties. The lines represent a simultaneous fit of the results with the empirical scaling formula in Equation ??..	80
178			
179			
180			
181			
182			
183	53	p_T -integrated yield ratios of strange and multi-strange hadrons to $(\pi^+ + \pi^-)$ as a function of $\langle dN_{ch}/d\eta_{lab} \rangle$ measured in the rapidity interval $ \eta < 0.5$. The empty and dark-shaded boxes show the total systematic uncertainty and the contribution uncorrelated across multiplicity bins, respectively. The values are compared to calculations from MC models and to results obtained in Pb–Pb and p–Pb collisions at the LHC.	81
184			
185			
186			
187			
188			

¹⁸⁹ **List of Tables**

190	1	Quantum numbers and masses associated to the three lighter quarks: u, d and s	17
191	2	Parameters used in the thermal-model calculations.	18
192	3	Properties of particles used in the ratio calculations.	19
193	4	Difference of mass (ΔM), baryon number (ΔB), strangeness (ΔS) and charge (ΔQ) of the ratios. The values of the slopes needs to be checked!!!! .	21
194	5	Number of accepted and analyzed events per multiplicity/centrality interval	43
195	6	Track selections common to all decay daughters and primary track selections applied to the charged pions from decays of Ξ^{*0}	43
196	7	Topological and track selection criteria.	44
197	8	Summary of the systematic uncertainties on the differential yield, $d^2N/(dp_T dy)$. Minimum and maximum values in all p_T intervals and multiplicity classes in p–Pb, centrality classes in Pb–Pb are shown for each source.	68
198			
199			
200			
201			
202			

203 1 The physics of relativistic heavy-ion collisions

204 1.1 Standard model

205 . Our current understanding concerning the question what the world is made of is collected
 206 in the Standard Model of particle physics (SM) [12], that describes our universe in terms of
 207 matter and forces. In this picture matter is composed of 12 point-like particles, which have a
 208 spin of 1/2 (fermions) and can be classified according to how they interact or equivalently to
 209 what charges they carry. There are six quarks (up, down, charm, strange, top and bottom)
 210 and six leptons (electron, electron neutrino, muon, muon neutrino, tau, tau neutrino) as
 211 reported in Figure `refig:sm`. The interactions between elementary particles are described
 212 by the exchange of gauge bosons (usually as virtual particles¹) or equivalently by mean of
 213 a field. Mathematically, the SM is a quantized Yang-Mills theory based on the non-abelian
 214 symmetry group $U(1) \rightarrow SU(2) \rightarrow SU(3)$ and has a total of twelve gauge bosons: the photon,
 215 three weak bosons and eight gluons. The interactions included in such a model are the
 216 electromagnetic force, the weak force and the strong one. Quarks have a property called
 217 color, playing the role of charge in the strong force. Both quarks and leptons are affected
 218 by the weak force and all the charged particles interact electromagnetically. The models
 219 that describe these interactions are listed as follows:

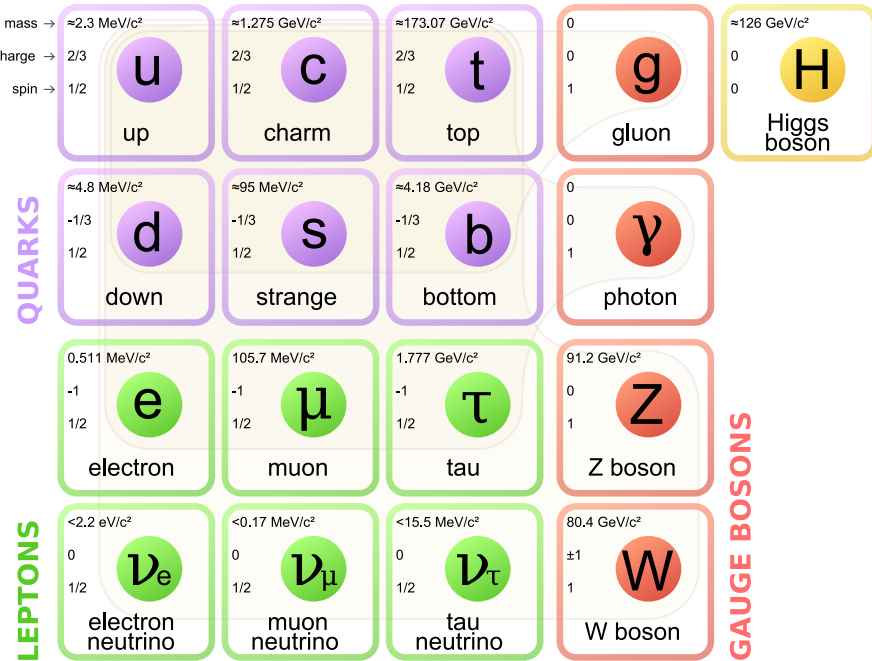


Figure 1: Standard Model families of leptons and quarks as the gauge bosons

220 **Quantum Electro-Dynamics (QED)** describes how light and matter interact. This
221 is the first theory where full agreement between quantum mechanics and special relativity
222 is achieved. It was developed between 1946 and 1950 by Tomonaga Shinichiro, Julian S.
223 Schwinger and Richard P. Feynmann. They were awarded the Nobel prize in 1965.

224
225 **Electroweak Theory (EW)** is the unified description of two of the four known funda-
226 mental interactions of nature: electromagnetism and the weak interaction. It first appeared
227 in 1961, driven by Sheldon Lee Glashow, and was completed in 1967 by Abdus Salam and
228 Steven Weinberg. They were awarded the Nobel prize in 1979. The first measurement
229 of the existence of the weak bosons W^+ , W^- and Z^0 was performed in 1983, when they
230 were produced and directly observed in $S\bar{p}\bar{p}S$ collisions at CERN. During the next year the
231 Nobel prize for this experimental result was assigned to Carlo Rubbia and Simon van der
232 Meer. In 1999 Gerardus 't Hooft and Martinus Veltman were awarded the Nobel prize for
233 showing that the electroweak theory is renormalisable.

234
235 **Quantum Chromo-dynamics (QCD)** is the theory of the strong interaction (color
236 force), describing the interactions between quarks and gluons which make up the hadrons.
237 Starting from the classification of the large amount of particles discovered during the fifties,
238 the original idea of the quark model by Gell-Mann (Nobel Prize in 1969) has been developed
239 during the sixties until 1973, when David J. Gross, H. David Politzer and Frank Wilczek
240 discovered the 'asymptotic freedom' property of the strong nuclear interaction (Nobel
241 Prize in 2004).

242 1.2 QCD and Quark-Gluon plasma

243 When, starting in 1950s, the number of known particle species became large, the idea
244 that these could be the elementary constituents of matter was replaced by the notion
245 that these species could in fact be composite objects made up of fewer, more elementary
246 particles, in a similar way to what had already happened to the elements of Mendeleev's
247 Periodic Table. The original idea by Gell-Mann (1964) was that the hadrons could be
248 obtained as combination of the fundamental representation of an $SU_f(3)$ group, where
249 three different flavors of quark ($q = u, d, s$) combine to build mesons ($q\bar{q}$) and hadrons
250 (qqq). However, when cataloging hadrons using the $SU_f(3)$ group, there are anomalous
251 states, such as the $\Omega^-(sss)$ and the $\Delta^{++}(uuu)$, that are combinations of three quarks of
252 the same flavor, in clear contrast with the Pauli exclusion principle for fermions. A solution
253 was proposed in 1965 by Moo-Young Han with Yoichiro Nambu and Oscar W. Greenberg,
254 who independently solved the problem by proposing that quarks possess an additional
255 $SU(3)$ gauge quantum number, later called color charge. This new quantum number may
256 assume three states, represented by the three primary colors: red, green and blue (denoted
257 symbolically by R, G and B, respectively). The introduction of this new quantum number
258 also provides an explanation to other empirical evidence, such as the fact that no qq , $\bar{q}q$

259 or the single quark have never been observed directly. On the other hand, the existence of
 260 color charge gives rise to the possible existence of differently colored states for each particle;
 261 thus, we could have many states for the proton, such as $u_R u_G d_B$, $u_R u_G d_G$, $u_B u_R d_R$, and
 262 so on. The fundamental rule that solves such contradictions is that all the particle states
 263 observed in nature are "colorless" or "white" (or, to be more precise, unchanged under
 264 $SU_c(3)$ rotations). The dynamics of the quarks and gluons are controlled by the gauge
 265 invariant QCD Lagrangian:

$$\mathcal{L}_{QCD} = \underbrace{i\delta_{ij}\bar{\Psi}_q^i\gamma^\mu\partial_\mu\Psi_q^j}_{\mathcal{L}_1} + \underbrace{g_s\bar{\Psi}_q^i\gamma^\mu t_{ij}^a A_\mu^a\Psi_q^j}_{\mathcal{L}_2} + \underbrace{m_q\bar{\Psi}_q^i\Psi_q^j}_{\mathcal{L}_3} + \underbrace{\frac{1}{4}F_{\mu\nu}^a F^{a\mu\nu}}_{\mathcal{L}_4} \quad (1)$$

266 where the coloured gluon field tensor, $F_{\mu\nu}^a$ (with color index a) and the squared gauge
 267 coupling parameter, g_s^2 (associated to the strong coupling constant α_s) are defined as:

$$F_{\mu\nu}^a = \partial_{mu}A_\nu^a - \partial_\nu A_\mu^a + g_s f^{abc} A_\mu^b A_\nu^c \quad (2)$$

268 and

$$g_s^2 = 4\pi\alpha_s \quad (3)$$

269 where:

- 270 • Ψ_q^i : the quark field with flavor q and color index $i \in [1;3]$, such as $\Psi_q = (\Psi_{qR}, \Psi_{qG},$
 271 $\Psi_{qB})^T$ and A_μ^a is the gluon field with color index a (adjoint representation)
- 272 • γ^μ : Dirac matrices that express the vector nature of the strong interaction, with μ
 273 being the Lorentz vector associated index
- 274 • m_q : quark mass, a priori not equal to zero (resulting from the Higgs mechanism or
 275 equivalent)
- 276 • t_{ij}^a : generator matrices of the group $SU_c(3)$, proportional to the Gell-Mann matrices,
 277 that perform revolutions in color space, representing interaction of quarks and gluons
- 278 • f^{abc} : structure constant of QCD

279 Each of the four terms of the QCD Lagrangian expresses and aspect of the interaction,
 280 specifically:

- 281 • \mathcal{L}_1 : gives the kinetic energy of the quark field Ψ_q^i
- 282 • \mathcal{L}_2 : gives the interaction between quarks (fermions) and gluons (the bosons of the
 283 interaction)
- 284 • \mathcal{L}_3 : gives the mass of the quarks

- 285 • \mathcal{L}_4 : gives the kinetic energy of the gluons

286 The terms of this equation, together with the fundamental parameters α_s and m_q ,
 287 summarize in just one expression all the features of the strong interaction. The first three
 288 terms describe the free propagation of quarks and gluons and the quark-gluon interaction.
 289 The remaining two terms show the presence of three and four gluon vertices in QCD and
 290 reflect the fact that gluons themselves carry color charge. This is a consequence of the non-
 291 abelian4 character of the gauge group. This peculiarity of the QCD interaction imposes the
 292 evolution of the strong coupling constant, α_s . The corresponding trend has been measured
 293 experimentally, and compared in Figure 2 with predictions. A practical consequence of
 294 this behavior is that the corresponding potential has a completely different shape than the
 295 other fundamental interactions and can be expressed by the following equation:

$$V(r) = -4 \frac{\alpha_s}{3r} + kr \quad (4)$$

296 where r is the separation distance between the two quarks and k is a constant that is
 297 approximately 1 GeV/fm.

298 Three are main properties of the QCD interaction:

299
 300 **Confinement** At large distances between quarks and gluons (i.e. small values of trans-
 301 ferred momentum Q in Figure 2) the coupling constant is large and the associated force
 302 is strong enough to keep these elementary con- stituents (usually called partons) confined
 303 in bounded states. As expressed in the Equation 4, the attractive potential increases with
 304 the increasing of the relative distance between the two partons preventing the separation
 305 of an individual quark or gluon. This explains the meaning of the term "confinement"
 306 adopted to describe this energy regime. From the theoretical point of view, the large value
 307 of α_s make impossible any perturbative approach in the solution of the Hamilton equation
 308 of the system. A successful solution is to perform the study of the system on a discrete
 309 space. Such techniques are known as lattice QCD and are based on numerical Monte Carlo
 310 simulations. The challenge for the calculations is to reduce the lattice spacing in order to
 311 approach the continuum.

312
 313 **Asymptotic freedom** Reducing the distance between quarks and gluons (i.e. increas-
 314 ing Q in Figure 2) the coupling constant α_s becomes smaller. As anticipated, this is a
 315 unique feature among the forces and comes from the non-abelian nature of the QCD gauge
 316 symmetry. Such a phenomenon is also depicted by the weakening of the anti-screening
 317 effect of the surround- ing virtual gluons with decreasing distance. In this way two quarks
 318 closer and closer in space show each other a smaller and smaller color charge. **Chiral**
 319 **symmetry** One further property of interest is connected to the chirality of the quark. It
 320 can be verified that the QCD lagrangian for massless quarks is invariant under a chiral
 321 rotation $(SU_L(N_f) \times SU_R(N_f))$, while the operator $\bar{q}q = \bar{q}_L q_R + \bar{q}_R q_L$ is not invariant (in

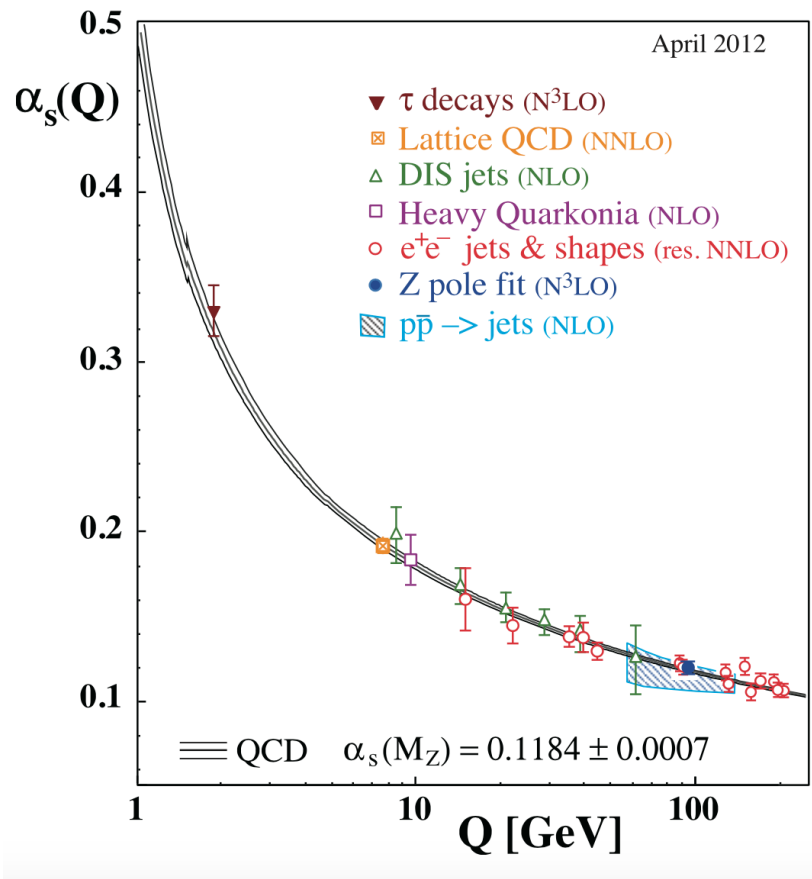


Figure 2: Summary of measurements of α_s as a function of the respective energy scale Q . The respective degree of QCD perturbation theory used in the extraction of α_s is indicated in brackets (NLO: next-to-leading order; NNLO: next-to-next-to leading order; res. NNLO: NNLO matched with resummed next-to-leading logs; N3LO: next-to-NNLO) [1]

322 the axial part), meaning that the mesons (state $\bar{q}q$) should have the same mass. Experi-
323 mentally this is clearly not true, and it could be shown that the axial current is conserved
324 (PCAC and the Goldberger-Treiman relation). The solution to this puzzle is that the chi-
325 ral (axial-vector) symmetry is spontaneously broken; this means that the symmetry of the
326 Hamiltonian is not a symmetry of the corresponding ground state. It has also been shown,
327 by G. t?Hooft, that the confinement implies a dynamical breaking of the chiral symmetry
328 [7]; this means that the breaking comes from the interaction between the objects in the
329 system. From this follows that the masses of the quarks are strongly increased because of
330 the interaction with the constituents of the system. This mechanism, known as dynamical
331 chiral symmetry breaking justifies the mass of the hadrons, reducing the role of the Higgs
332 mechanism in the mass explanation at least for the light hadrons.

333 **1.3 Heavy Ion Collisions**

334 In the case a QGP is formed, it will eventually expand because of its internal pressure.
335 As the system expands it also cools. The space-time evolution of the expansion can be
336 seen in Figure 3 (right side). A and B represent the two incoming ion beams. After a pre-
337 equilibrium phase a QGP is formed. As it expands, the system will eventually reach what
338 is known as the critical temperature (T_c). At this point partons begin to hadronize and this
339 will continue until the chemical freeze-out (T_{ch}) takes place, when inelastic collisions cease.
340 At this stage the distribution of hadrons is frozen. As cooling and expansion continue the
341 hadrons reach what is called thermal freeze out (T_{fo}). Here the elastic collisions stop and
342 the hadrons carry fixed momenta. The QGP state can not be directly observed, because of
343 its short lifetime. Instead, through experiment we measure the final state hadrons, which
344 have a fixed momentum after T_{fo} . The observables of interest should tell us about the
345 de-confinement and the thermodynamic properties of the matter. Moreover, experimental
346 measurements include yields and p_T spectra of various particle species, azimuthal studies
347 of high p_T particles, phase space distributions, and particle correlations.

348 A practical way to reach a critical condition in which a nuclear system should undergo
349 a phase transition to the QGP, at high temperature and/or matter density, is to collide
350 two nuclei at sufficiently high energy. Therefore, relativistic and ultra-relativistic heavy-ion
351 collisions are a unique tool to study nuclear matter under extreme conditions.

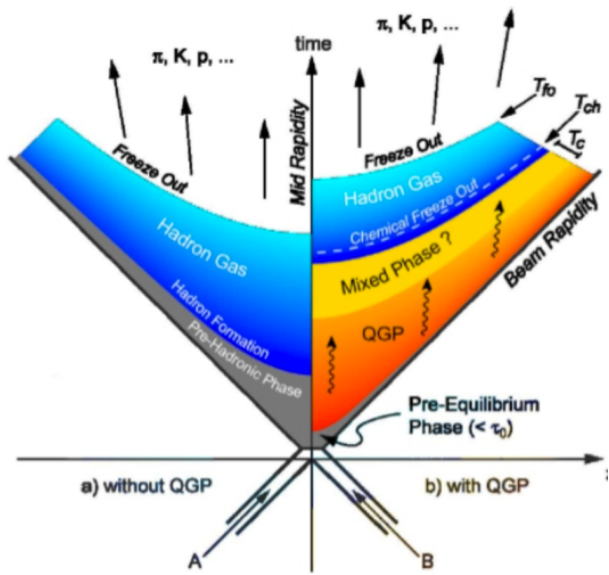


Figure 3: Hydrodynamic evolution of a heavy ion collision with and without the formation of a QGP.

352 2 Production of resonance with strangeness

353 The Quark Model, proposed independently by Murray Gell-Mann and Yuval Ne?eman in
354 1964 [?], enables the classification of hadrons in terms of their constituent quarks. In
355 this model, the lighter mesons and baryons are representations of an $SU_f(3)$ group, whose
356 fundamental representation is the three dimensional vector (u, d, s). These are the three
357 lighter quarks whose characteristics are reported in Table `reftable:quark`.

Light flavor	d	u	s
Baryon number (B)	+1/3	+1/3	+1/3
Electric charge (Q)	-1/3	+2/3	-1/3
Isospin (I)	-1/2	+1/2	0
Strangeness (S)	0	0	-1
mass (MeV/c^2)	$2.3^{+0.7}_{-0.5}$	$4.8^{+0.5}_{-0.3}$	95 ± 5

Table 1: Quantum numbers and masses associated to the three lighter quarks: u, d and s

358 The hadronic state are obtained from the decomposition of the following scalar prod-
359 ucts of the fundamental representations of the group:

360
361 Meson ($q\bar{q}$) $3 \otimes \bar{3} = 1 \oplus 8$

362
363 Baryon (qqq) $3 \otimes 3 \otimes 3 = 10 \oplus 8 \oplus 8 \oplus 1$

365 2.1 Strange quark and hyperons

366 2.2 Resonance prodction

367 3 Theoretical models

368 3.1 Thermal statistical model

369 The statistical-thermal model has proved extremely successful in applications to relativistic
370 collisions of both heavy ions and elementary particles. In light of this success, THERMUS,
371 a thermal model analysis package, has been developed for incorporation into the object-
372 oriented ROOT framework [13].

373
374 There are three types of statistical-thermal models in explaining data in high energy nu-
375 clear physics and THERMUS treats the system quantum numbers B (baryon number), S
376 (strangeness) and Q (charge) within three distinct formalisms:

- 377 1. **Grand-Canonical Ensemble:** Because the hot dense matter produced in nucleus-
- 378 nucleus collisions is large enough, this ensemble is the most widely used in applications
- 379 to heavy-ion collisions, in which the quantum numbers are conserved on average.
- 380 2. **Fully-Canonical Ensemble:** In which B, S and Q are each exactly conserved and
- 381 this ensemble used in high-energy elementary collisions such as pp, p \bar{p} and e $^-$ e $^+$
- 382 collisions.
- 383 3. **Strangeness-Canonical Ensemble:** In small systems or at low temperatures, a
- 384 canonical treatment leads to a suppression of hadrons carrying non-zero quantum
- 385 numbers, since these particles have to be created in pairs and the resulting low
- 386 production of strange particles requires a canonical treatment of strangeness.

387 In order to calculate the thermal properties of a system, one starts with an evaluation

388 of its partition function. The form of the partition function obviously depends on the

389 choice of ensemble. In the present analysis the strangeness-canonical ensemble used and

390 the statistical-thermal model requires six parameters as input: the chemical freeze-out

391 temperature T , baryon and charge chemical potentials μ_B and μ_Q respectively, canonical

392 or correlation radius, R_C ; the radius inside which strangeness is exactly conserved and the

393 fireball radius R . An additional strangeness saturation factor γ_S has been used as indicator

394 of a possible departure from equilibrium and $\gamma_S = 1.0$ corresponds to complete strangeness

395 equilibration.

396 The volume dependence cancels out when studying the particle ratios as well as strangeness

397 canonical equivalent to grand canonical formalism if $\Delta S = 0$ in the ratios and γ_S also can-

398 celes out. Parameters used in the analysis listed in Table 2. The μ_B parameter taken from

399 the Ref. [14].

Table 2: Parameters used in the thermal-model calculations.

Parameter	Value
T (MeV)	varied (see text)
μ_B (MeV)	$9.2 \times 10^{-2}????$
μ_Q (MeV)	0.0
γ_S	1.0

400

401 **3.1.1 Calculations**

402 *Concept:*

403 In order to calculate the particle ratios within strangeness canonical formalism of THER-
 404 MUS, temperature varied between 60 MeV to 180 MeV and particle yields extracted for
 405 each temperature value and then primary particle ratios calculated for each case.

406

407 *Feed-Down Correction:*

408 Since the particle yields measured by the detectors in collision experiments include feed-
 409 down from heavier hadrons and hadronic resonances, the primordial hadrons are allowed to
 410 decay to particles considered stable by the experiment before model predictions are com-
 411 compared with experimental data. In the analysis only Λ particles counted as stable (do not
 412 allowed to decay) so there is no feed-down contribution from these particles to the other
 413 ratios.

414

415

416 Properties of studied particles and their particle ratios listed in Table 3 and Table 4,
 417 respectively.

Table 3: Properties of particles used in the ratio calculations.

Particle	Δ^{++}	p	K^{*0}	K^0	K^+	Λ^*	Λ	Σ^{*+}	Σ^+	Σ^0
Mass (MeV/c^2)	1232	938.27	895.92	497.61	493.67	1519.5	1115.68	1382.8	1189.37	1192.6
Width (MeV/c^2)	120	–	50.7	–	–	15.6	–	37.6	–	–
$c\tau$ (fm)	1.6	–	3.9	–	–	12.6	–	5.51	–	–
Ang. Momentum (J)	3/2	1/2	1	1	0	3/2	1/2	3/2	1/2	1/2
Isospin (I)	3/2	1/2	1/2	1/2	1/2	0	0	1	1	1
Parity (P)	+1	+1	-1	-1	0	-1	+1	+1	+1	+1
Strangeness (S)	0	0	1	1	1	-1	-1	-1	-1	-1
Baryon Number (B)	1	1	0	0	0	1	1	1	1	1
Decay Channel	$p\pi^+$	–	π^-	–	$\mu^+\nu_\mu$	pK^-	$p\pi^-$	$\Lambda\pi^+$	$p\pi^0$	$\Lambda\gamma$
Branching Ratio (%)	~ 100	–	~ 66.7	–	~ 63.54	~ 45	~ 63.9	~ 87	~ 51.6	~ 100
Q-Value(MeV/c^2)	154.16	–	262.68	–	–	87.55	37.84	127.55	111.53	76.96

418

419

420 **3.1.2 Results**

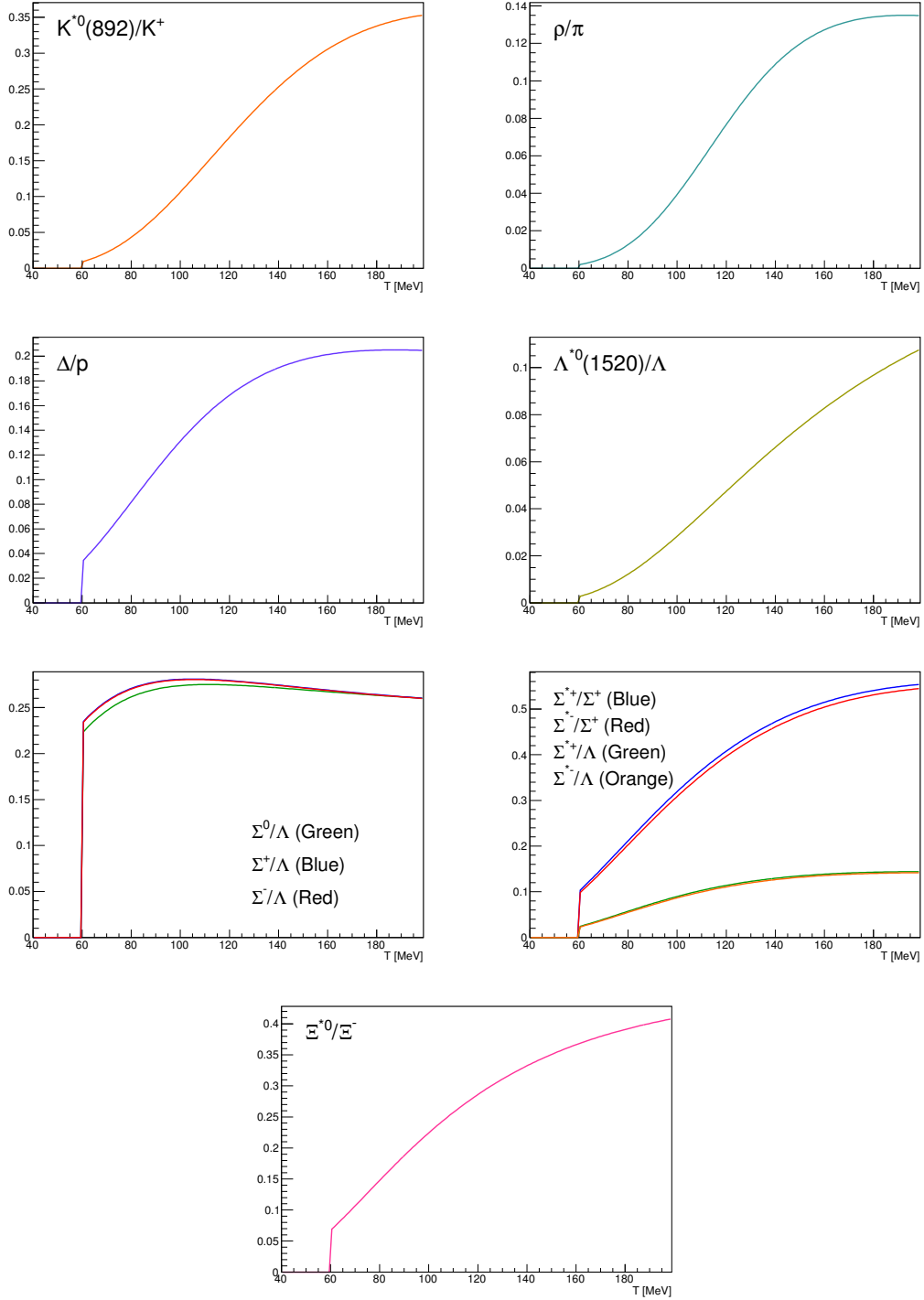


Figure 4: Ratio of baryonic and mesonic resonances over their stable partner as a function of temperature.

Table 4: Difference of mass (ΔM), baryon number (ΔB), strangeness (ΔS) and charge (ΔQ) of the ratios. The values of the slopes needs to be checked!!!!

Particle	Δ^{++}/p	K^*/K^+	Λ^*/Λ	Σ^{*+}/Λ	Σ^{*+}/Σ^0	Σ^0/Λ	Σ^{*+}/Σ^+	Ξ^{*0}/Ξ^-
ΔM (MeV/ c^2)	293.8	402.25	403.82	267.12	190.16	76.96	193.43	210.49
ΔB	0	0	0	0	0	0	0	0
ΔS	0	0	0	0	0	0	0	0
ΔQ	+1	-1	0	+1	0	+1	0	-1
Slope (%) per MeV ????????	0.19	0.76	0.98	0.25	-	-0.08	0.37	0.42

421 **3.1.3 Comparison with data**

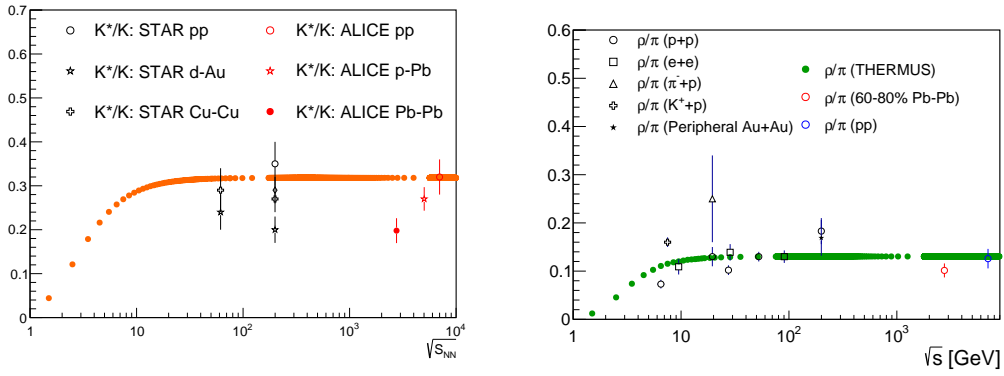


Figure 5: Ratio of resonances over their stable partner as a function of $\sqrt(s)$.

422 **3.2 UrQMD**

423 **4 A Large Ion Collider Experiment at the LHC**

424 ALICE (A Large Ion Collider Experiment) has been collecting data during the whole first
425 phase of the Large Hadron Collider operations, from its startup on the 23 November 2009
426 to the beginning of the first long technical shutdown in February 2013. During the first
427 three years of operations LHC provided pp collisions at 0.9, 2.76, 7 and 8 TeV, Pb–Pb colli-
428 sions at 2.76A TeV and finally p–Pb collisions at 5.02 TeV. The first section of this chapter
429 focuses on the LHC performance during this phase and includes details on the accelerator
430 parameters that allow the LHC to perform as a lead ion collider. A detailed description
431 of the ALICE detector follows in the section 4.2.1. ALICE has been designed and op-
432 timized to study the high particle-multiplicity environment of ultra-relativistic heavy-ion
433 collisions and its tracking and particle identification performance in Pb–Pb collisions are
434 discussed. The attention is drawn in particular on the central barrel detectors. Section
435 4.2.2 describes the ALICE Data Acquisition (DAQ) system, that also embeds tools for the
436 online Data Quality Monitoring (DQM). The final part of the chapter is dedicated to the
437 offline computing and reconstruction system based on the GRID framework.

438 **4.1 The Large Hadron Collider**

439 The Large Hadron Collider (LHC) [15] at CERN is the biggest particle accelerator world-
440 wide. The LHC project was approved in 1994 and construction works in the existing
441 underground tunnel started in 2001 after the dismantling of the LEP collider, which had
442 previously been built in the tunnel which is located under the Swiss-French border area
443 close to Geneva at a depth of 50 to 175 m. The LHC has a circumference of 26.7 km. By
444 design, its maximum achievable energies are 7 TeV for beam of protons and 2.76 TeV per
445 nucleon for beam of lead ions, thus providing collisions at $\sqrt{s} = 14$ TeV and $\sqrt{s_{NN}} = 5.5$
446 TeV, respectively. These would be the largest energies ever achieved in particle collision
447 experiments. The LHC is a synchrotron that accelerates two counter-rotating beams in
448 separate parallel beam pipes. In each of them bunches of particles travel many times
449 around the accelerator ring before the collision energy is reached. The accelerator has to
450 bend the beams around the ring, keep the bunches focused and accelerate them to their
451 collision energy. Finally, the spatial dimension of the bunches has to be minimized in order
452 to attain high luminosity, which ensure a high number of collisions per time interval at
453 the collision points, i.e. a high luminosity. A combination of magnetic and electric field
454 components performs the mentioned tasks. Despite the high luminosity reached, only a
455 very small fraction of the particles of two bunches collides in a single bunch crossing. The
456 others leave the interaction region essentially uninfluenced, are defocused, and continue to
457 circulate in the accelerator.

458 Injection of bunches into the LHC (Figure 6) is preceded by acceleration in the LINAC2,
459 PS booster, PS, and SPS accelerators. The acceleration sequence is slightly different for
460 heavy-ions, in which case bunches pass the LINAC3, LEIR, PS, and SPS accelerators

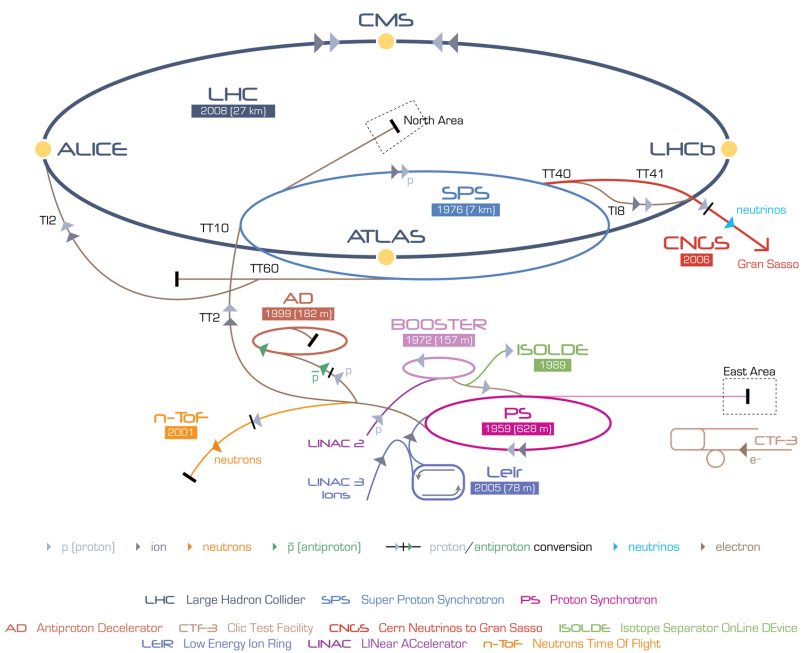


Figure 6: The CERN accelerator complex [2]

461 (more information can be found in [90]). Several injections to the LHC are needed until all
462 bunches of both beams are filled. The first pp collisions at 900 GeV centre-of-mass energy
463 were delivered by the LHC on September 10th 2008. Nine days later, the operations were
464 interrupted due to a failure in an electrical connection between two magnets. The machine
465 operators spent over a year repairing and consolidating the accelerator. On November
466 20th 2009 low energy proton beams circulated again, and a few days later, by achieving
467 the energy of 1.18 TeV per proton beam, LHC became the most powerful accelerator in the
468 world. The first pp collisions at centre-of-mass energy of 7 TeV were delivered in March
469 2010, and the first Pb?Pb collisions at centre-of-mass energy of 2.76 TeV per nucleon pair
470 in November 2010. In 2010 the integrated luminosity delivered by the LHC was $\sim 48 \text{ pb}^{-1}$
471 for pp collisions at $\sqrt{s} = 7 \text{ TeV}$ ($\sim 0.5 \text{ pb}^{-1}$ in ALICE) and $\sim 10 \mu\text{b}^{-1}$ for Pb?Pb at $\sqrt{s_{\text{NN}}} =$
472 2.76 TeV ($\sim 10 \mu\text{b}^{-1}$ in ALICE). In 2011 the beam energy was the same as in 2010 both
473 for pp and Pb–Pb. The performance of the LHC improved in terms of luminosity with \sim
474 5.61 fb^{-1} for pp ($\sim 2 \text{ pb}^{-1}$ in ALICE) and $\sim 166 \mu\text{b}^{-1}$ for Pb–Pb collisions ($\sim 143.62 \mu\text{b}^{-1}$
475 in ALICE). In 2012, the centre-of-mass energy for pp collisions was brought to 8 TeV and
476 the integrated luminosity (up to December 2012, end of the pp program) was $\sim 23.3 \text{ fb}^{-1}$
477 ($\sim 10 \text{ pb}^{-1}$ in ALICE). A pilot p–Pb run operated at $\sqrt{s_{\text{NN}}} = 5.02 \text{ TeV}$ on September 2012,
478 followed by a long p–Pb run on February 2013 with a delivered luminosity of 31.2 nb^{-1} . A
479 very short pp run at $\sqrt{s} = 2.76 \text{ TeV}$ ended the Run1 of the LHC program, marking the start
480 of the first long shutdown (LS1) until the end of 2014. Despite its excellent performance,
481 the LHC has not yet achieved the nominal parameters (\sqrt{s}, L), that is the main goal for
482 the next ignition of the machine in 2015. The LHC produces collisions in four so called
483 Interaction Points (IPs) in correspondence of which are located six detectors of different
484 dimensions and with different goals, all able to study the products of the interactions.
485 These are:

486
487 **ALICE (A Large Ion Collider Experiment-IP₂)** [16] is a dedicated heavy-ion ex-
488 periment designed to study strongly-interacting matter at very high energy density. It
489 explores the phase transition to the QGP, its phase diagram, and its properties. Further-
490 more, ALICE will also study collisions of protons, on one hand as a baseline for heavy-ion
491 measurements and on the other hand it contributes to measurements of identified particles
492 by making use of its excellent particle identification capability and its acceptance at very
493 low transverse momenta.

494
495 **ATLAS (A Toroidal LHC ApparatuS-IP₁) and CMS (Compact Muon Solenoid**
496 **- IP₅)** [17][18] are general-purpose detectors for pp collisions that are built to cover the
497 widest possible range of physics at the LHC. Specific topics are the search for the Higgs
498 boson and physics beyond the Standard Model, e.g. new heavy particles postulated by
499 supersymmetric extensions (SUSY) of the Standard Model and evidence of extra dimensions.

500
501 **LHCb (The Large Hadron Collider beauty experiment-IP₈)** [19] is a dedicated

502 experiment for the study of heavy flavor physics at the LHC. In particular, the experiment
503 focuses on the study of CP violation and rare decays of beauty and charm particles, to
504 test the Standard Model and to search for evidence of New Physics. The LHCb physics
505 program is complementary to the flavor physics studies conducted at the B-factories and
506 to the direct searches for new particles performed at ATLAS and CMS.

507

508 **LHCf (Large Hadron Collider forward experiment-IP₁)** [20] measures forward
509 particles created during LHC collisions to provide further understanding of high energy
510 cosmic rays. The detector is placed close to the ATLAS experiment.

511

512 **TOTEM (TOTal Elastic and diffractive cross-section Measurement-IP₅)** [21]
513 measures the total cross-section, elastic scattering, and diffractive processes. The detector
514 is located close to the CMS experiment.

515

516 4.2 The ALICE project

517 The ALICE experiment at the LHC [22] has as main goal the study of nuclear matter
518 under extreme conditions of temperature and energy density such as those reached in ultra-
519 relativistic heavy-ion collisions. The aim is to verify the QCD prediction of the existence of
520 a phase transition from the common hadronic matter to the Quark-Gluon Plasma. Since
521 ALICE is the only LHC experiment specifically designed for Pb–Pb collisions, it has to
522 be able to cope with the large multiplicities associated with these collision systems and at
523 the same time has to cover as many QGP-related observables as possible. ALICE is also
524 interested in the study of pp interactions, as these are crucial for a comparison with Pb–Pb
525 collisions, to tune Monte Carlo models and per se, like the other LHC experiments. With
526 respect to these experiments, ALICE is endowed with an excellent Particle IDentification
527 (PID) performance, obtained combining different PID techniques from different detectors
528 that are optimized in different momentum (p) regions.

529 4.2.1 ALICE detector

530 ALICE is a complex of 14 detector subsystems (Figure 7) that can be classified in three
531 groups:

532

533 **Central detectors** are housed in a solenoid magnet which provides the experiment
534 with a 0.5 T magnetic field and covers the pseudo-rapidity interval $-0.9 < \eta < 0.9$ (corre-
535 sponding to a polar acceptance $\pi/4 < \theta < 3\pi/4$). The azimuthal acceptance is 2π . They
536 are mainly dedicated to vertex reconstruction, tracking, particle identification and momen-
537 tum measurement. Starting from the interaction region and going outward, we find the
538 following detectors:

- 539 • Inner Tracking System (ITS)
 540 • Time Projection Chamber (TPC)
 541 • Transition Radiation Detector (TRD)
 542 • Time Of Flight (TOF)

543 In the mid-rapidity region there are also three detectors with limited azimuthal accep-
 544 tance:

- 545 • High Momentum Particle Identification Detector (HMPID)
 546 • PHOton Spectrometer (POHS)
 547 • ElectroMagnetic CALorimeter (EMCAL)

548 **Muon spectrometer** is placed in the forward pseudo-rapidity region ($-4.0 < \eta < -2.5$) and consists of a dipole magnet and tracking and trigger chambers. It is optimized to
 549 reconstruct heavy quark resonances (such as J/Ψ through their $\mu^+\mu^-$ decay channel) and
 550 single muons.

552 **Forward detectors** are placed in the high pseudo-rapidity region (small angles with
 553 respect to the beam pipe). They are small and specialized detector systems used for
 554 triggering or to measure global event characteristics. They are:

- 556 • Time Zero (T0) to measure the event time with precision of the order of tens of
 557 picoseconds, as needed by TOF
 558 • VZERO (V0) to reject the beam-gas background and to trigger minimum bias events
 559 • Forward Multiplicity Detector (FMD) to provide multiplicity information over a large
 560 fraction of the solid angle ($-3.4 < \eta < -1.7$ and $1.7 < \eta < 5$)
 561 • Photon Multiplicity Detector (PMD) to measure the multiplicity and the spatial
 562 distribution of photons on an event-by-event basis in the $2.3 < \eta < 3.7$ region
 563 • Zero Degree Calorimeter (ZDC) to measure and trigger on the impact parameter. The
 564 ZDC consists of two calorimeters, one for neutrons (ZDC:ZN) and one for protons
 565 (ZDC:ZP), and includes also an electromagnetic calorimeter (ZEM)

566 The ALICE global coordinate system [23] is a right-handed orthogonal Cartesian system
 567 with the origin X, Y, Z = 0 at the centre of the detector. The three Cartesian axes are
 568 defined as follows: the X axis pointing towards the centre of the LHC, the Y axis pointing
 569 upward and the Z axis parallel to the local mean beam line pointing in the direction opposite

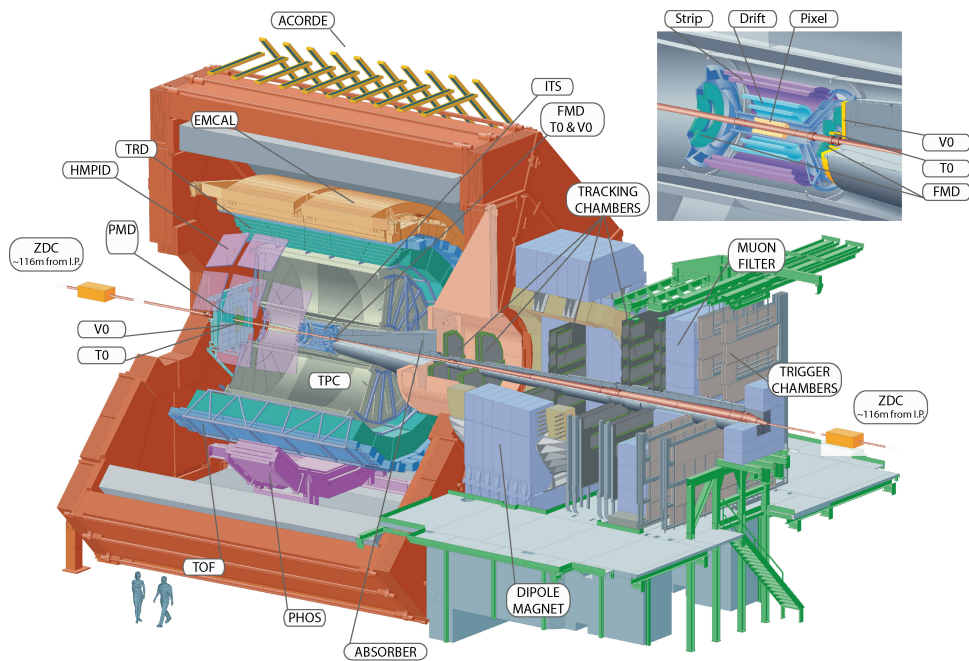


Figure 7: The ALICE detector

570 to the muon spectrometer. The azimuthal angle increases counter-clockwise from the
571 positive X axis ($\Phi = 0$) to the positive Y axis ($\Phi = \pi/2$) with the observer standing at
572 positive Z and looking at negative Z; the polar angle increases from the positive Z axis (θ
573 = 0) to the X-Y plane ($\theta = \pi/2$) and to the negative Z axis ($\theta = \pi$).

574 In the following Sections more specific descriptions of the detectors used in the identifi-
575 cation of the $\Xi(1530)^0$ baryons and in the determination of the characteristics of typical
576 collisions will be given.

577

578 ITS

579 The ITS [22] (Figure 8) is the barrel detector closest to the beam pipe. Its main goals are:

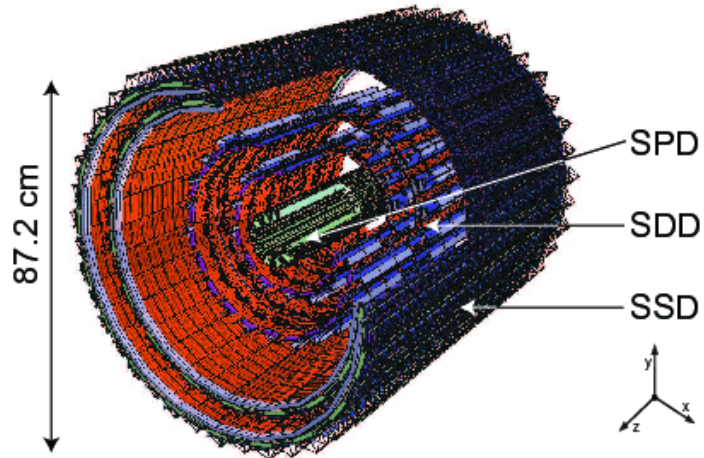


Figure 8: Schematic view of the ITS [3]

580

- 581 • to contribute with the TPC to the global tracking of ALICE by improving the angle
582 and momentum resolution
- 583 • to reconstruct the position of the primary interaction vertex
- 584 • to reconstruct secondary vertices from decays of heavy-flavor and strange particle
585 decays;
- 586 • to track and identify particles with momentum below $100 \text{ MeV}/c^2$
- 587 • to improve the momentum, impact parameter and angle resolution for the measure-
588 ment of high p_T particles performed with the TPC

- 589 • to reconstruct particles traversing dead regions of the TPC

590 The ITS surrounds the beam pipe (which is a 800 μm thick cylinder with an outer
 591 diameter of 2.9 cm) and consists of six cylindrical layers of silicon detectors located at radii
 592 between 4 cm and 43 cm. Due to the high track density, the two innermost layers are
 593 Silicon Pixel Detectors (SPD) which guarantee a high granularity. They are followed by
 594 two layers of Silicon Drift Detectors (SDD), while the two outmost layers are double-sided
 595 Silicon micro-Strip Detectors (SSD).

596 Since the momentum and impact parameter resolutions for low momentum particles
 597 are dominated by multiple scattering effects, the amount of material in the active volume
 598 has been minimized as much as possible. The granularity of the detector was optimized to
 599 keep the occupancy low in all the layers. With the technology chosen, the ITS detectors
 600 reach a spatial resolution of the order of a few tens of m resulting in a resolution on the
 601 impact-parameter⁵ better than 70 m in the r plane for $p_T > 1 \text{ GeV}/c$ and thus well suited
 602 for the reconstruction of heavy-flavor decays (see Figure 9).

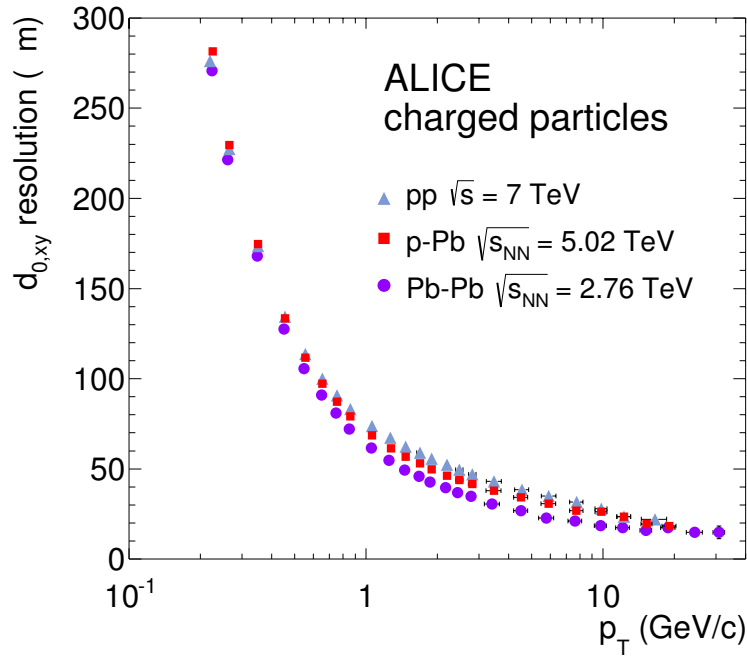


Figure 9: Track impact parameter resolution in the transverse plane ($r\phi$) vs p_T for charged particle

603 TPC

604 The TPC [24] (Figure 10) is the main tracking detector of the central barrel, optimized

605 to provide, together with the other central barrel detectors, charged- particle momentum
 606 measurements with good two-track separation, particle identification and vertex determina-
 607 tion. The TPC was designed for an excellent tracking performance in the high multiplicity
 608 environment of Pb–Pb collisions. For this reason, it was chosen to be a drift chamber,
 609 cylindrical in shape, 5 m long, with the inner radius ($r_{in} \sim 85$ cm) determined by the
 610 maximum acceptable track density, and the external one ($r_{ext} \sim 250$ cm) by the minimum
 611 track length for which dE/dx resolution is $< 10\%$. The TPC volume is filled with 90 m^3 of
 612 Ne/CO₂/N₂ (90/10/5). The readout planes are divided in 18 sectors in which multi-wire
 613 proportional chambers (with cathode pad readout) are housed. Because of its good dE/dx
 614 resolution, the TPC can identify particles with $p_T < 1\text{ GeV}/c$ on a track-by-track basis.

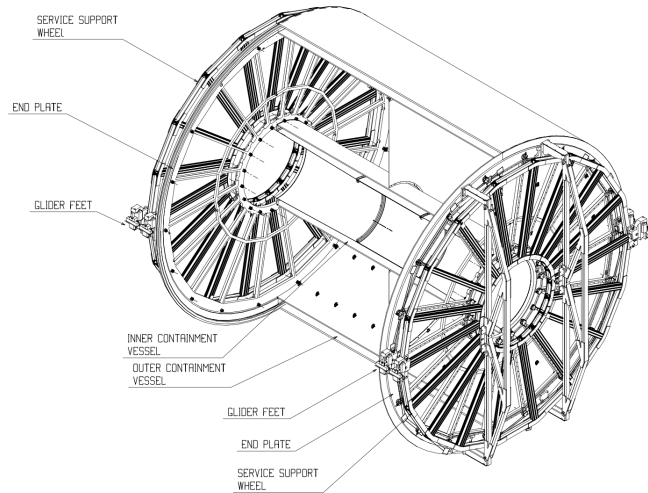


Figure 10: Schematic view of the TPC

615 Charged particles traveling through the TPC ionize the detector's gas; the measure-
 616 ment of this loss of energy is what we need to identify a particle. The physics observable
 617 in this case is the energy loss per unit length, within the matter crossed by the charged
 618 particle, which we call specific energy loss, also denoted by dE/dx . This is described by
 619 the Bethe–Bloch equation, 5, that highlights the key of the identification technique: this
 620 observable depends only on the charge and on velocity (β) of the particle, which, in turn,
 621 depends only on the momentum and the mass of the ionizing particle. Since momentum is
 622 already known due to track curvature and charge is unitary for most measured tracks, mea-
 623 suring the dE/dx allows us to indirectly determine mass and thus determine the particle
 624 species. The Bethe-Bloch equation gives the mean specific energy loss:

$$-\langle \frac{dE}{dx} \rangle = k_1 \cdot z^2 \frac{Z}{A} \cdot \frac{1}{\beta^2} \left[\frac{1}{2} \ln(k_2 \cdot m_e c^2 \cdot \beta^2 \gamma^2) - \beta^2 + k_3 \right] \quad (5)$$

625 where $\beta\gamma = p/Mc$ and: Z: atomic number of the ionized gas (in this case Ne/CO₂/N₂)
 626 A: mass number of the ionized gas (g/mol)
 627 m_e : electron mass
 628 z: electric charge of the ionizing particle in unit of electron charge e
 629 M: ionizing particle mass
 630 p: ionizing particle momentum
 631 β : ionizing particle velocity normalized to the light velocity c
 632 $\gamma = 1/\sqrt{1 - \beta^2}$, Lorentz factor
 633 k_1, k_2, k_3 : constants depending on the ionized medium
 634

635 For a given ionizing particle mass hypothesis, a given momentum and a given length
 636 of the trajectory in the ionizing medium, the total charge deposited along the trajectory
 637 is subject to statistical fluctuations. This random variable follows a Landau distribution,
 638 that give us the opportunity to measure the mean value hdE/dx . The long tail of the
 639 Landau distribution is usually truncated at 50%-70% of the collected signal.

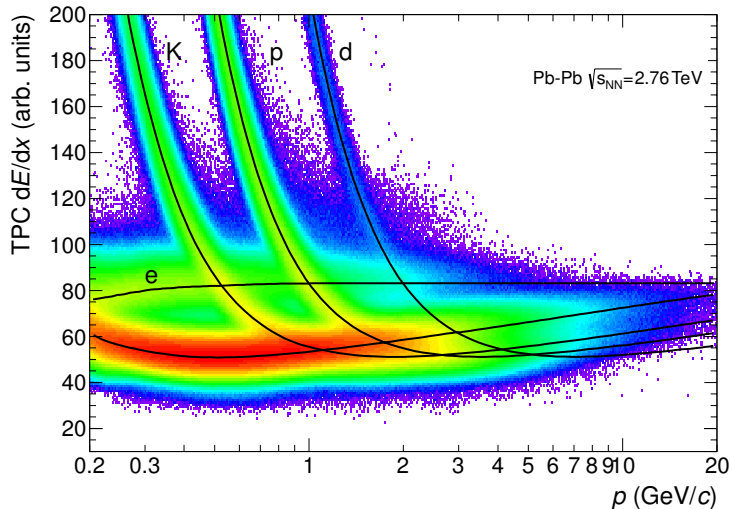


Figure 11: Specific energy loss (dE/dx) in the TPC vs. particle momentum in Pb–Pb collisions at $\sqrt{s_{NN}} = 2.76$ TeV. The lines show the parametrisations of the expected mean energy loss.

640 The specific energy loss in the TPC as a function of momentum is shown in Figure
 641 11. The different bands characteristic for $e^\pm, \pi^\pm, K^\pm, p^\pm$ are clearly visible. These
 642 are the evidence of the statistical distribution of the measured energy loss around the
 643 expected mean value. The expected value correspond to the prediction by a Bethe–Bloch
 644 experimental parametrization (superimposed as black lines in the Figure). For a track

645 within the TPC the relevant quantity to be considered for PID is the difference between
 646 the measured specific energy loss and the corresponding predicted value, by the Bethe-
 647 Bloch parametrization for a given measured momentum. If normalized to the resolution
 648 of the dE/dx measurement in the TPC, this difference could be expressed in number of
 649 σ (see Equation 6). In this way it is possible to estimate more quantitatively the goodness
 650 of a mass hypothesis. This also gives us the possibility to choose the strictness we want to
 651 adopt in the identification of a particle (n_σ , $n = 2, 3, 4$):

$$n_\sigma = \frac{(dE/dx)_{measured} - (dE/dx)_{Bethe-Bloch}}{\sigma_{TPC}} \quad (6)$$

V0

652 The VZERO detector [25] consists of two segmented arrays of plastic scintillator counters,
 653 called VZERO-A and VZERO-C, placed around the beam-pipe on either side of the IP:
 654 one at $Z = 340$ cm, covering the pseudo-rapidity range [2.8; 5.1], and the other at $Z = -90$
 655 cm (in front of the absorber), covering the pseudo-rapidity range [-3.7; -1.7]. They consist
 656 of 32 counters distributed in four rings, each divided in eight 45 sectors. Each counter
 657 is made of scintillator material embedded with WaveLength Shifting fibers. Clear fibers
 658 collect and transport the signal to photomultipliers 3 - 5 m far from the detector, inside
 659 the L3 magnet. The counters have a time resolution better than 1 ns. Their response is
 660 recorded in a time window of 25 ns around the nominal beam crossing time. The VZERO
 661 has an important role in rejecting background from beam-gas collisions (see, Figure 12)
 662 exploiting the relative time-of-flight measurement between the two arrays: when the beam-
 663 gas collision takes place outside the region between the two arrays, particles arrive 6 ns
 664 before or after the time of a beam-beam collision.

665 The VZERO is a trigger detector that will provide a minimum-bias trigger for all
 666 colliding systems to the central barrel detectors and three centrality triggers in p-Pb and
 667 Pb-Pb collisions (multiplicity, central and semi-central).

668 The first parameter to be determined in A-A (p-A) collisions is the centrality (multiplicity).
 669 This is defined according to the value of the impact parameter, b , and provides a geomet-
 670 rical scale of the overlapping region between the colliding nuclei: a collision will be defined
 671 from central to peripheral, as the impact parameter increases. The centrality of a collision
 672 is not directly available and must be deduced from a combination of experimentally mea-
 673 sured quantities and Monte Carlo simulations. There are a number of observables that can
 674 be measured and used as centrality estimators. The charged-particle multiplicity N_{ch} and
 675 the transverse energy E_T measured around mid-rapidity are measurable quantities related
 676 to the energy deposited in the interaction region (these are therefore related to N_{part}).
 677 These variables increase significantly increasing the centrality of the collisions. Another
 678 measurable quantity to estimate the centrality is the zero-degree energy EZDC, namely
 679 the energy carried by spectator nucleons $N_{spec} = 2A - N_{part} = E_{ZDC}/E_A$, where E_A is
 680 the beam energy per nucleon. Typically a measured distribution of one of the previous
 681 observables is mapped to the corresponding distribution obtained from phenomenological

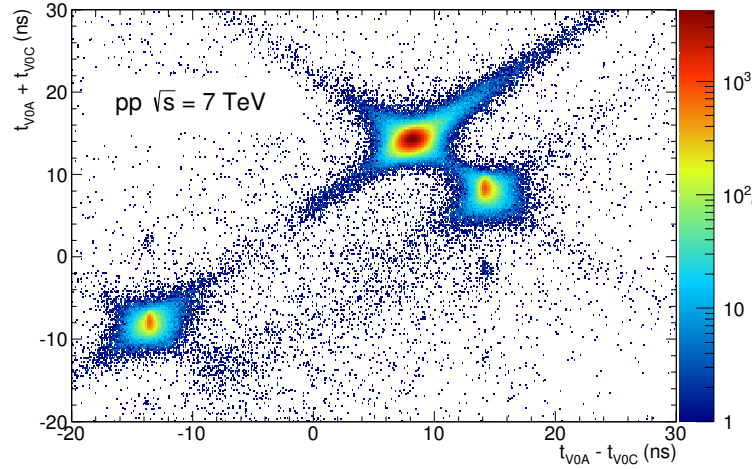


Figure 12: Correlation between the sum and difference of signal times in V0A and V0C. Three classes of events collisions at (8.3 ns, 14.3 ns), background from Beam 1 at (-14.3 ns, -8.3 ns), and background from Beam 2 at (14.3 ns, 8.3 ns) can be clearly distinguished.

683 Glauber calculations. The Glauber model [26, 27] uses a semi-classical approach: the A?A
 684 collision is assumed to be an incoherent superposition of N elementary nucleon- nucleon
 685 collisions. The main parameters of the model are the inelastic nucleon- nucleon collision
 686 cross-section σ_n and the nuclear density distribution $\rho(r)$. In practice, the simulated dis-
 687 tribution well reproduce the measured distribution or the latter is fitted with an analytical
 688 function. The experimental distribution can then be divided in classes with sharp cuts on
 689 the measured observable (E_{ZDC} , E_T or N_{ch}). These "centrality" classes will correspond to
 690 well defined percentage of the integral of the distribution. A given centrality class in the
 691 measured distribution, corresponds to the same class in the simulated distribution, where
 692 the main geometrical variables (N_{part} , N_{coll} and T_{AA}) can be determined. The number of
 693 classes that can be defined depends on the resolution achievable on the selection variable.
 694 In the analysis described in this thesis the centrality(multiplicity) estimation is based on
 695 the measurement of the multiplicities from the VZERO scintillators [28][29]. This is the
 696 method that achieve the best centrality resolution: it ranges from 0.5% in central to 2%
 697 in peripheral collisions. Other methods, as the ones based on the E_{ZDC} measurement or
 698 based on the estimate of the number of tracks in the SPD or TPC, are used to asses a
 699 systematic uncertainty on the centrality determination. The distribution of the VZERO
 700 amplitudes is shown in Figure 13 where the centrality(multiplicity) percentiles are also
 701 indicated.

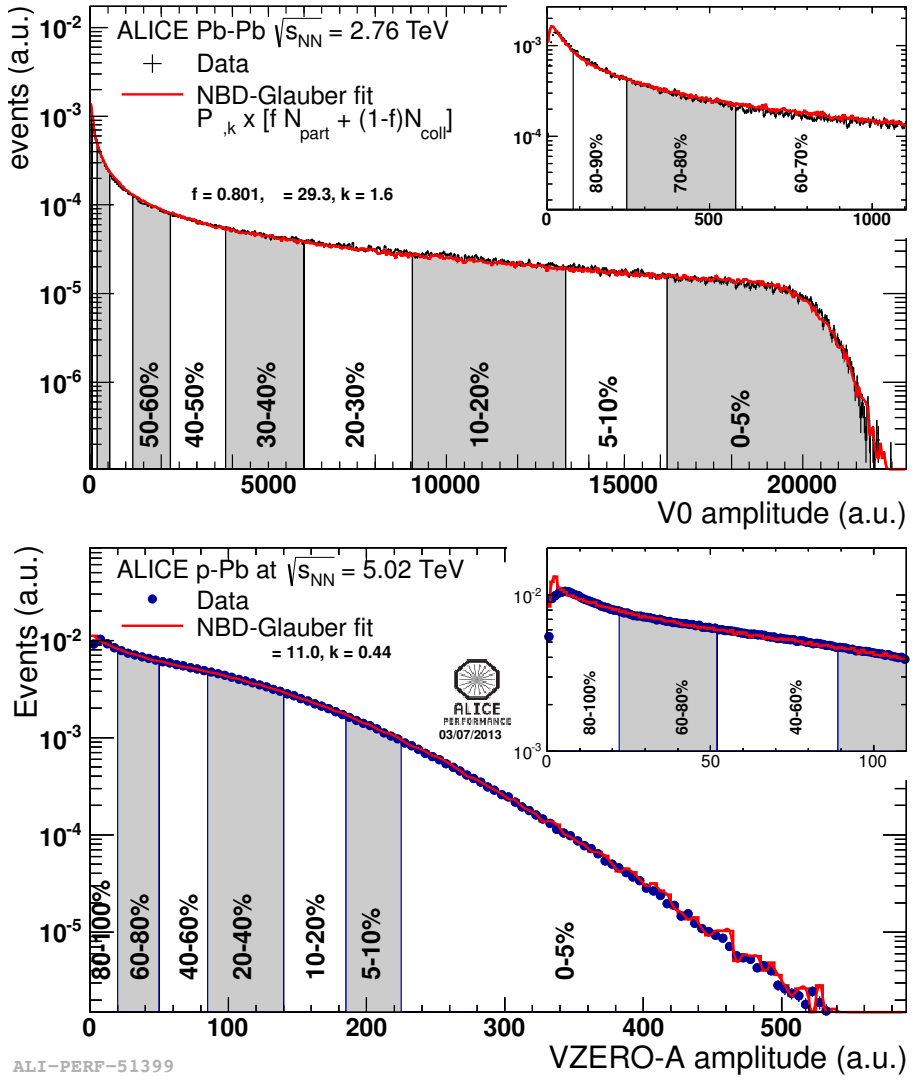


Figure 13: Distribution of the V0 amplitude (sum of V0A and V0C in top, V0A in bottom). The inset shows a magnified version of the most peripheral region.

4.2.2 Data Acquisition (DAQ) and trigger system

703 The architecture of data acquisition is shown in Figure 14. The tasks of the ALICE DAQ
 704 system are the assembly of event informations from individual detectors into complete
 705 events (event building) as well as buffer- ing and export of assembled events to permanent
 706 storage. The DAQ is designed to process a data rate up to 1.25 GB/s in heavy-ion runs.
 707 Event building is done in two steps. Data from the detectors is received by Detector Data
 708 Links (DDLs) on Local Data Concentrators (LDCs). The LDCs assemble the data into
 709 sub-events that are then shipped to Global Data Collectors (GDCs). A GDC re- ceives all
 710 sub-events from a given event and assembles them into a complete event. These events are
 711 subsequently stored on a system called Transient Data Storage (TDS).

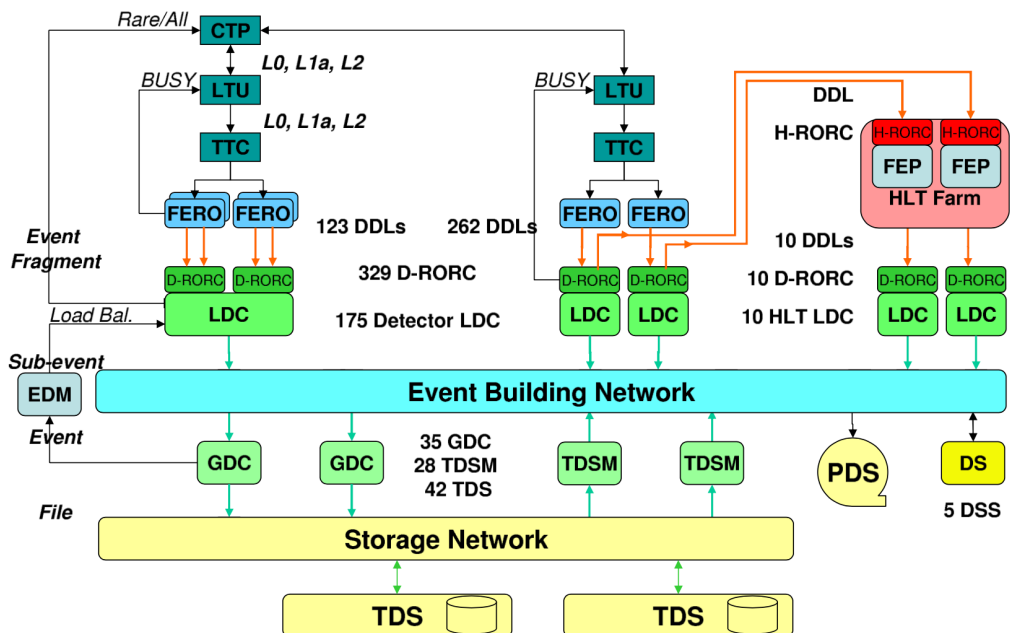


Figure 14: The overall architecture of the ALICE DAQ and the interface to the HLT system.

712 ALICE can simultaneously take data in several partitions, where a set of detectors
713 can store their outputs. Since a partition is a group of commonly controlled detectors, a
714 given detector can only be active in one partition at a time. The active detectors in a
715 given partition may be assigned to data taking groups called clusters, for which triggers

716 can be defined. Therefore, upon a trigger only a sub-set of the whole partition may
717 be read out. Furthermore, a triggering detector does not have to be necessarily part of
718 the partition. ALICE has a two-layer trigger architecture [30]. The low-level trigger is a
719 hardware trigger called Central Trigger Processor (CTP). The High-Level Trigger (HLT)
720 is implemented as a pure software trigger. The CTP combines inputs from different trigger
721 sources, namely the various detectors. These inputs are single signals, like a hit in the
722 detector, or, can be the result of fast calculation performed directly in the detectors. The
723 HLT allows the implementation of sophisticated logic for the triggering. In contrast to the
724 CTP which governs the readout of the detectors, the HLT receives a copy of the data read
725 out from the detectors and processes them. The hardware trigger combines the trigger
726 signals of the various detectors to decide if an event is accepted, that means it is read out
727 and written to disk. Several trigger levels reduce the event rate depending on the input
728 signals. The first level, called L0, is delivered after 1.2 ?s, while the second, called L1,
729 after 6.5 ?s. The final trigger, L2, is delivered after 100 ?s, upon completion of the drift
730 time in the TPC. Only after an L2 trigger the event is finally stored. The rates of different
731 trigger classes are very different. By definition minimum-bias triggers have the highest
732 rate; other triggers that look for rare signals are characterized by much lower rates. In
733 order to cope with different scenarios, downscaling factors can be applied to the trigger
734 classes individually, i.e. only every nth event fulfilling the trigger condition is read out. The
735 total recording rate is limited by the maximum bandwidth of data that can be recorded
736 to disk and tape. The ALICE software trigger, called HLT, is a farm of multiprocessor
737 computers. The aim is to have about 1000 PCs processing the data in parallel allowing
738 an online analysis of the events. A trigger decision comes from the analysis of a more
739 comprehensive set of information than what happens for the hardware trigger, giving the
740 possibility to apply more sophisticated triggers. Examples include triggers on high energy
741 jets or on muon pairs. Furthermore, the HLT can significantly reduce the event size by
742 selecting regions of interest (partial readout of detectors) and by further compression of the
743 data. The HLT receives a copy of the raw data and performs per detector reconstruction,
744 partly aided by hardware coprocessors. Subsequently, the trigger decision is based on the
745 global reconstructed event. In the same step a region of interest can be selected. In the
746 last optional step, if the trigger decision is positive, the data are compressed. The trigger
747 decision, partial readout information, compressed data, and the re- construction output
748 is sent to LDCs and subsequently processed by the DAQ. In terms of the overall DAQ
749 architecture, data sent by HLT is treated like stemming from a detector.

750 **4.2.3 ALICE offline software frame work**

751 The required computing resources for the reconstruction and analysis of the raw data as
752 well as the production of simulated events needed for the understanding of the data exceed
753 the computing power of single institutes and even centers like CERN. Therefore, institutes
754 that are part of the Collaboration also provide storage and computing resources. Distribu-
755 tion of the data for reconstruction and analysis cannot be performed manually and this
756 led to the need for an automated system. The concept of a decentralized computing model
757 called Grid [31] was identified as a solution.

758

759 *The AliEn Framework*

760 The Grid paradigm implies the unification of resources of distributed computing center,
761 in particular computing power and storage, to provide them to users all over the World.
762 It allows computing center to offer their resources to a wider community and the local re-
763 sources to be shared by an entire collaboration. Software that implements the Grid concept
764 is called Grid middleware. ALICE has developed a Grid middleware called AliEn [32] since
765 2001. An ALICE user employs AliEn to connect to the ALICE Grid which is composed
766 of a combination of general services that are provided by many Grid middleware solutions
767 and ALICE-specific services provided by AliEn. Parts of the ALICE Grid are: i) a global
768 file catalog that is a directory of files in storage elements distributed over the Globe, ii)
769 the automatic matching of jobs for execution to a suitable location in one of the connected
770 sites, iii) a shell-like user interface and iv) API9 services for the ROOT framework [33].

771

772 *AliRoot Framework*

773 AliRoot [22] is the offline framework for simulation, alignment, calibration, reconstruction,
774 visualization, quality assurance, and analysis of experimental and simulated data. It is
775 based on the ROOT framework. Most of the code is written in C++ with some parts in
776 Fortran that are wrapped inside C++ code. Re-usability and modularity are the basic
777 features of the AliRoot framework. Modularity allows parts of the code to be replaced,
778 with minimum or no impact on the rest (for example changing the event generator, the
779 transport Monte Carlo or the reconstruction algorithms). This is achieved implementing
780 abstract interfaces. In addition codes for each detector subsystem are independent modules
781 with their specific code for simulation and reconstruction and the code can be developed
782 concurrently with minimum interference. Re-usability is meant to maintain a maximum
783 amount of backward compatibility as the system evolves.

784 The central module of the AliRoot framework is STEER (Figure 15) which provides
785 several common functions such as: steering of program execution for simulation, reconstruc-
786 tion and analysis; general run management, creation and destruction of data structures,
787 initialization and termination of program phases; base classes for simulation, event genera-
788 tion, reconstruction, detectors elements. For event simulation the framework provides the
789 following functionality:

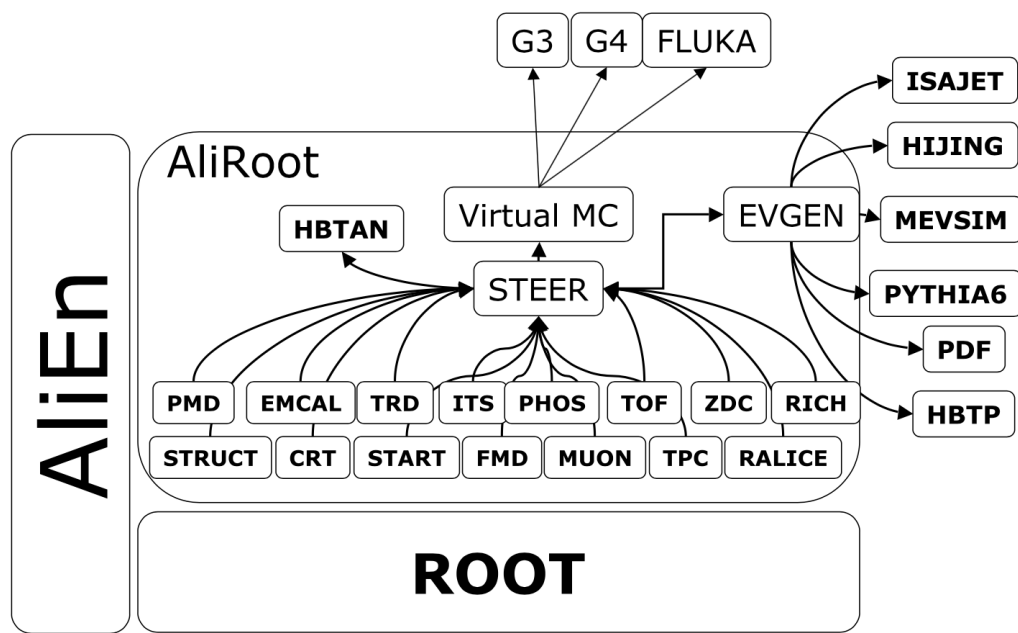


Figure 15: Schematic view of the AliRoot framework

790 **5 Measurement of $\Xi(1530)^0$ production in p–Pb and Pb–Pb**

791 The measurement of resonance production in p–Pb collisions helps to disentangle cold
792 nuclear matter effects from genuine hot medium effects and contribute to the study of
793 the system size dependence of re-scattering in the hadronic phase. And the measurement
794 in ultra-relativistic heavy-ion collisions such as Pb–Pb collisions, provide information on
795 the properties of hadronic medium and different stage of its evolution. In order to study
796 the particle production mechanism in the hadronic phase between the chemical and ki-
797 netic freeze-out, the $\Xi(1530)^0$ resonance production at mid-rapidity ($-0.5 < y_{\text{CMS}} < 0$) is
798 measured in p–Pb collisions $\sqrt{s_{\text{NN}}} = 5.02$ TeV and in Pb–Pb collisions with $|y| < 0.5$ at
799 $\sqrt{s_{\text{NN}}} = 2.76$ TeV with the ALICE experiment, via the reconstruction of its hadronic decay
800 into $\Xi\pi$.

801 **5.1 $\Xi(1530)^0$ -reconstruction**

802 The Ξ^{*0} production in p–Pb and Pb–Pb collisions at mid-rapidity has been studied in dif-
803 ferent multiplicity classes, from very central to peripheral collisions. The analysis strategy
804 is based on the invariant mass study of the reconstructed pairs (referred to as the candi-
805 dates) whose provenance could be the decay of a Ξ^{*0} baryon into charged particles. The
806 decay products (also called daughters in the text) are identified as oppositely charged Ξ and
807 π among the tracks reconstructed in the central barrel. The event selection, track selec-
808 tion and the particle identification strategy is described. The raw signal yield is extracted
809 by fitting the background-subtracted invariant mass distribution in several transverse mo-
810 mentum intervals. In order to extract the p_{T} -dependent cross section, these yields are
811 corrected for efficiency. The p_{T} -dependent correction due to the detector acceptance and
812 reconstruction efficiency, $(\text{Acc} \times \epsilon_{\text{rec}})(\text{pt})$, is computed from a Monte Carlo simulation.
813 The absolute normalisation is then performed, by dividing for the number of the events in
814 each multiplicity and centrality classes.

815 **5.1.1 Data sample and event selection**

816 A description of the ALICE detector and of its performance during the LHC Run 1 (2010–
817 2013) can be found in [22, 34]. The data sample in the analysis from Pb–Pb collisions with
818 energy of $\sqrt{s_{\text{NN}}} = 2.76$ obtained during 2011 and the sample of p–Pb run at $\sqrt{s_{\text{NN}}} = 5.02$
819 TeV was recorded in 2013.

820 Due to the asymmetric energies of the proton (4 TeV) and lead ion (1.57 A TeV) beams,
821 the centre-of-mass system in the nucleon-nucleon frame is shifted in rapidity by $\Delta y_{\text{NN}} =$
822 0.465 towards the direction of the proton beam with respect to the laboratory frame of
823 the ALICE detector [5]. For the analysed p–Pb data set, the direction of the proton beam
824 was towards the ALICE muon spectrometer, the so-called “C” side, standing for negative
825 rapidities; conversely, the Pb beam circulated towards positive rapidities, labelled as “A”

826 side in the following. The analysis in this paper was carried out at midrapidity, in the
827 rapidity window $-0.5 < y_{\text{CMS}} < 0$.

828 The minimum-bias trigger during the p–Pb run was configured to select events by
829 requiring a logical OR of signals in V0A and V0C [34], two arrays of 32 scintillator detectors
830 covering the full azimuthal angle in the pseudo-rapidity regions $2.8 < \eta_{\text{lab}} < 5.1$ and
831 $-3.7 < \eta_{\text{lab}} < -1.7$, respectively [35]. In the data analysis it was required to have a
832 coincidence of signals in both V0A and V0C in order to reduce the contamination from
833 single-diffractive and electromagnetic interactions. Out of this sample in p–Pb collision
834 events about 109.3 million events, 93.9 million events satisfy the following selection criteria
835 and have been actually used for the analysis.

836 The Pb–Pb collisions data sample was selected by online centrality trigger requiring a
837 signal in the forward V0 detectors[29] to record enhanced data in central collision. The
838 data consists of 24.8 million events in most central collisions (0-10%), 21.8 million events in
839 semi-central collisions (10-50%) and 3.5 million events with minimum-bas trigger (0-90%).
840 Among 49.6 million events in total, 43.0 million events have been analyzed as passed the
841 criteria below.

- 842 • Events with z-coordinate of primary vertex (V_z) falling within ± 10 cm from the
843 interaction point
- 844 • Rejection of pile-up event
- 845 • Requiring primary tracks to have at least one hit in one of the two innermost layers
846 of the ITS (silicon pixel detector, SPD)
- 847 • p–Pb: multiplicity ranges in percentile (V0A): 0-20%, 20-40%, 40-60%, 60-100% and
848 MB(0-100%)
- 849 • Pb–Pb: centrality classes (V0A and V0C): 0-10%, 10-40%, 40-80% and MB (0-80%)

850 The distribution of the vertex z position of the accepted events in p–Pb collision is
851 reported on left panel in Figure 16 and corresponding figure but obtained from Pb–Pb
852 collisions is shown on right panel in Figure. 16. Events with $|V_z| < 10$ cm have been used
853 to ensure a uniform acceptance in the central pseudo-rapidity region, $|\eta| < 0.8$, where the
854 analysis is performed. This cut reduces the total number of events to 97.5 million events,
855 that is the $\sim 89.2\%$ of the initial sample in p–Pb collisions and 43.04 million events which
856 is $\sim 86.8\%$ of the initial sample in Pb–Pb collisions are survived.

857 Fig. 17 shows the multiplicity distribution of the accepted events in p–Pb collision
858 divided in bins of percentile. The each color on the histogram indicate the multiplicity
859 ranges used in this analysis. Corresponding events for each multiplicity range are in Table
860 5.

861 The distribution of centrality in each trigger used to select the events in Pb–Pb collision
862 is shown in Fig. 18 and the reason why the centrality has step structure is that there are

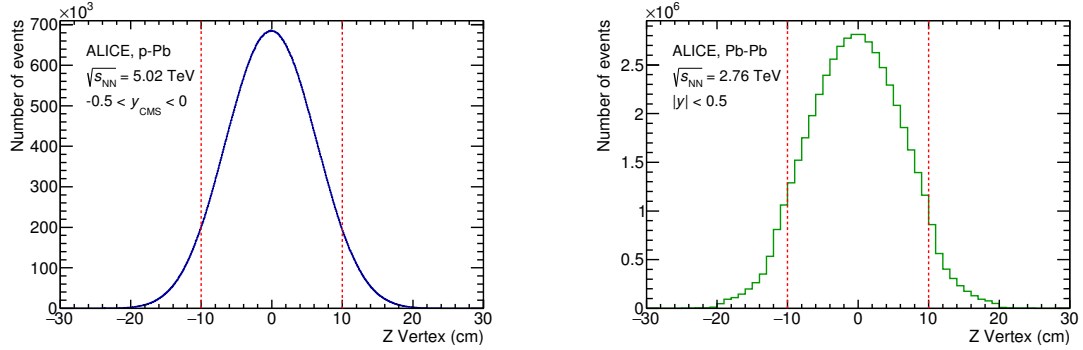


Figure 16: Vertex-z coordinate distribution of the accepted events in p–Pb collision(Left) and in Pb–Pb collisions(Right). The red dashed line indicates vertex cut

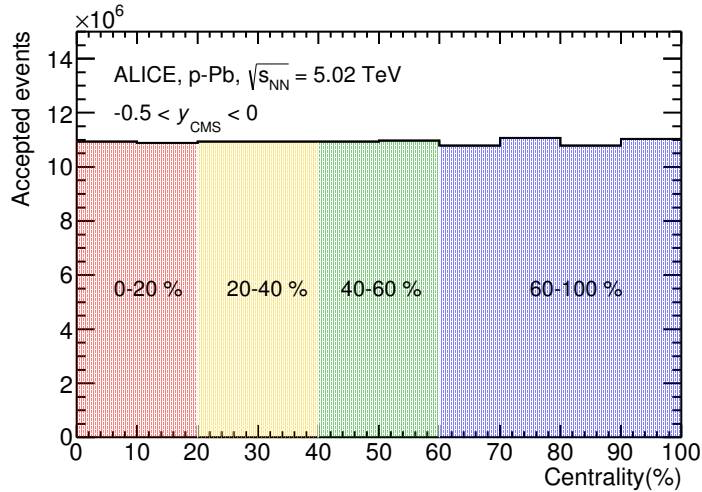


Figure 17: Multiplicity distribution of accepted events in p–Pb collision in percentile. The each color and labels define the four intervals in which the analysis is performed.

863 three different trigger classes classified by the amplitude threshold on VZERO detector.
 864 Because the distribution of events as function of centrality is not a flat, this may lead to
 865 additional bias, in particular when one needs to combine the results from different triggers.
 866 For example, events from 40-80% centrality bin have bias with high statistics in 40-60%. In
 867 order to avoid this effect, we have applied a flattening procedure to have flat distribution
 868 of events as function of centrality. A brief explanation of the method is below :

- 869 1. Histograms are obtained for the effective mass distribution in 1% centrality bins and
 870 for the centrality distribution
- 871 2. The effective mass distributions are scaled in each 1% centrality bin by a factor:
 872 Factor = $N_{\text{event}} \text{ in 20-40\%} / 20 / N_{\text{event}} \text{ in current 1\% bin}$
- 873 3. Each bin in the centrality distribution is scaled using the factor described above
- 874 4. Histograms are added for centrality bins of interest: 0-10%, 10-40%, 40-80%, 0-80%

875 The resulting number of events in each centrality classes is summarized in Table 5.

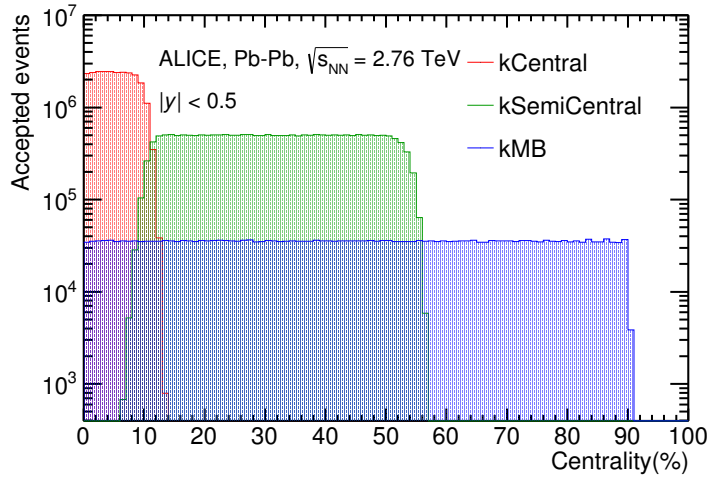


Figure 18: Centrality distribution of three different trigger classes.

p-Pb	0-20%	21.82×10^6
	20-40%	21.86×10^6
	40-60%	21.91×10^6
	60-100%	43.68×10^6
Pb-Pb	0-10%	5.58×10^6
	10-40%	16.73×10^6
	40-80%	22.31×10^6

Table 5: Number of accepted and analyzed events per multiplicity/centrality interval

876 **5.1.2 Track and topological selection**

877 In comparison with the Ξ^{*0} analysis carried out in pp collisions at $\sqrt{s} = 7$ TeV [7], track
 878 and topological selections were revised and adapted to the p-Pb dataset. Pions from strong
 879 decays of Ξ^{*0} were selected according to the criteria for primary tracks. As summarized
 880 in Table 6, all charged tracks were selected with $p_T > 0.15$ GeV/c and $|\eta_{\text{lab}}| < 0.8$,
 881 as described in Ref. [34]. The primary tracks were chosen with the Distance of Closest
 882 Approach (DCA) to PV of less than 2 cm along the longitudinal direction (DCA_z) and
 883 lower than $7\sigma_r$ in the transverse plane (DCA_r), where σ_r is the resolution of DCA_r . The σ_r
 884 is strongly p_T -dependent and lower than 100 μm for $p_T > 0.5$ GeV/c [34]. To ensure a good
 885 track reconstruction quality, candidate tracks were required to have at least one hit in one
 886 of the two innermost layers (SPD) of the ITS and to have at least 70 reconstructed points in
 887 the Time Projection Chamber (TPC), out of a maximum of 159. The Particle IDentification
 888 (PID) criteria for all decay daughters are based on the requirement that the specific energy
 889 loss ($\text{d}E/\text{d}x$) is measured in the TPC within three standard deviations (σ_{TPC}) from the
 expected value ($\text{d}E/\text{d}x_{\text{exp}}$), computed using a Bethe-Bloch parametrization [34].

Common track selections	$ \eta_{\text{lab}} $	< 0.8
	p_T	> 0.15 GeV/c
	PID $ (\text{d}E/\text{d}x) - (\text{d}E/\text{d}x)_{\text{exp}} $	$< 3 \sigma_{\text{TPC}}$
Primary track selections	DCA_z to PV	< 2 cm
	DCA_r to PV	$< 7\sigma_r$ - $10\sigma_r$ (p_T)
	number of SPD points	≥ 1
	number of TPC points	> 70
	χ^2 per cluster	< 4

Table 6: Track selections common to all decay daughters and primary track selections applied to the charged pions from decays of Ξ^{*0} .

890
 891 Since pions and protons from weak decay of Λ ($c\tau = 7.89$ cm [1]) and pions from weak
 892 decay of Ξ^- ($c\tau = 4.91$ cm [1]) are produced away from the PV, specific topological and

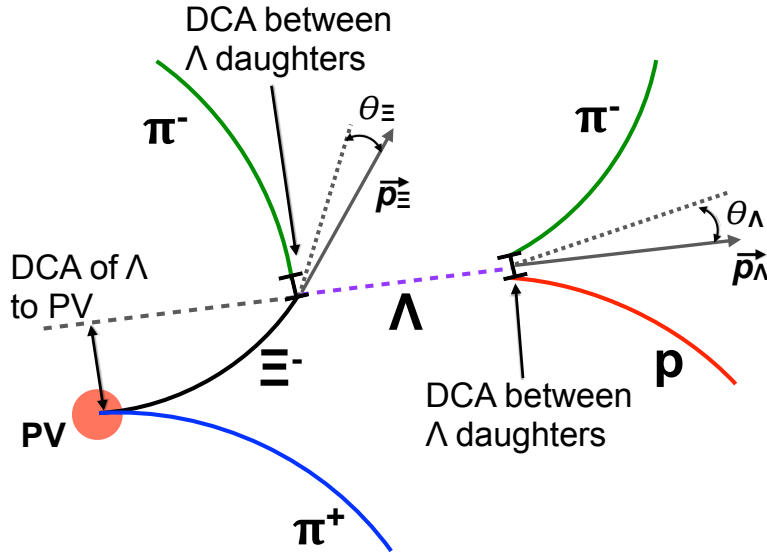


Figure 19: Sketch of the decay modes for Ξ^{*0} and depiction of the track and topological selection criteria.

893 track selection criteria, as summarized in Table 7, were applied [6, 7, 36].

Topological cuts	p-Pb	Pb-Pb
DCA _r of Λ decay products to PV	> 0.06 cm	> 0.11 cm
DCA between Λ decay products	< 1.4 cm	< 0.95 cm
DCA of Λ to PV	> 0.015 cm	> 0.06
$\cos\theta_\Lambda$	> 0.875	> 0.998
$r(\Lambda)$	$0.2 < r(\Lambda) < 100$ cm	$0.2 < r(\Lambda) < 100$ cm
$ M_{p\pi} - m_\Lambda $	$< 7 \text{ MeV}/c^2$	$< 7 \text{ MeV}/c^2$
DCA _r of pion (from Ξ^-) to PV	> 0.015 cm	> 0.035 cm
DCA between Ξ^- decay products	< 1.9 cm	< 0.275
$\cos\theta_\Xi$	> 0.981	> 0.9992
$r(\Xi^-)$	$0.2 < r(\Xi^-) < 100$ cm	$0.2 < r(\Xi^-) < 100$ cm
$ M_{\Lambda\pi} - m_\Xi $	$< 7 \text{ MeV}/c^2$	$< 7 \text{ MeV}/c^2$

Table 7: Topological and track selection criteria.

894 In the analysis of Ξ^{*0} , Λ and π from Ξ^- were selected with a DCA of less than 1.9 cm
 895 and with a DCA_r to the PV greater than 0.015 cm. The Λ daughter particles (π and p)

896 were required to have a DCA_r to the PV greater than 0.06 cm, while the DCA between the
897 two particles was required to be less than 1.4 cm. Cuts on the invariant mass, the cosine
898 of the pointing angle ($\theta_\Lambda, \theta_\Xi$) and the radius of the fiducial volume ($r(\Lambda), r(\Xi)$) in Table 7
899 were applied to optimize the balance of purity and efficiency of each particle sample.

900 **5.1.3 Particle identification**

901 PID selection criteria are applied for

- 902 1. π^\pm (last emitted π) and proton from Λ
 903 2. π^\pm (second emitted π) from Ξ^\pm
 904 3. π^\pm (first emitted π) from $\Xi(1530)^0$

905 by using TPC. On TPC dE/dx versus momentum distribution, 3σ cuts are applied to TPC
 906 for selecting each of the particles. The TPC dE/dx selection allows to have better signal
 907 with $\sim 20\%$ increase of significance.

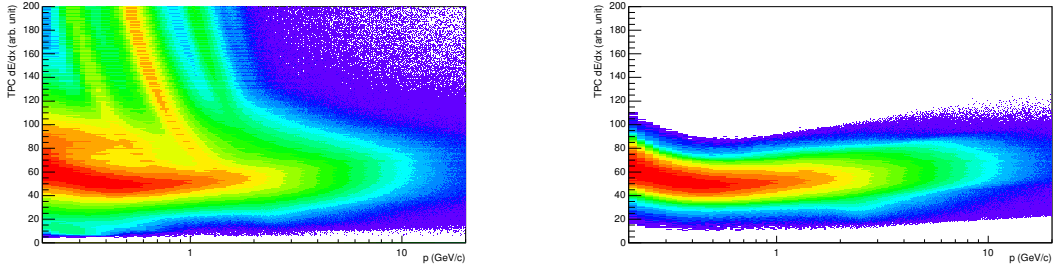


Figure 20: TPC dE/dx as function of transverse momentum for total (top) and selected first emitted π in 3σ (bottom)

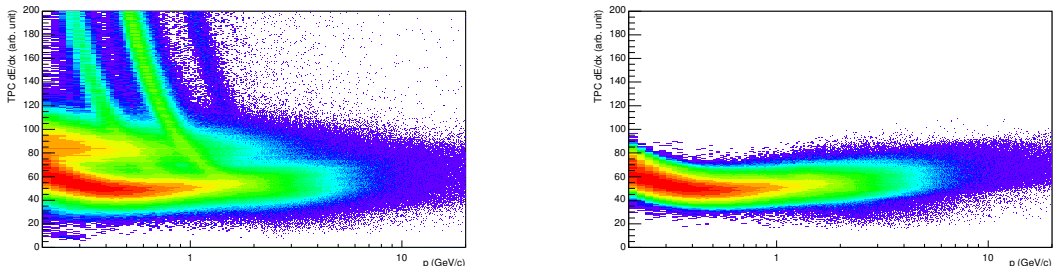


Figure 21: TPC dE/dx as function of transverse momentum for total (top) and selected second emitted π in 3σ (bottom)

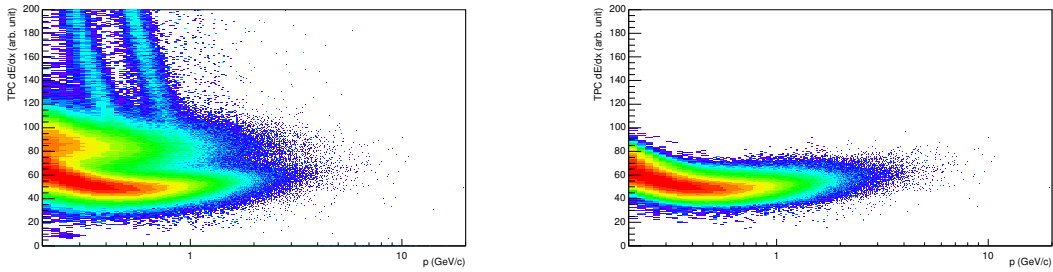


Figure 22: TPC dE/dx as function of transverse momentum for total (top) and selected last emitted π in 3σ (bottom)

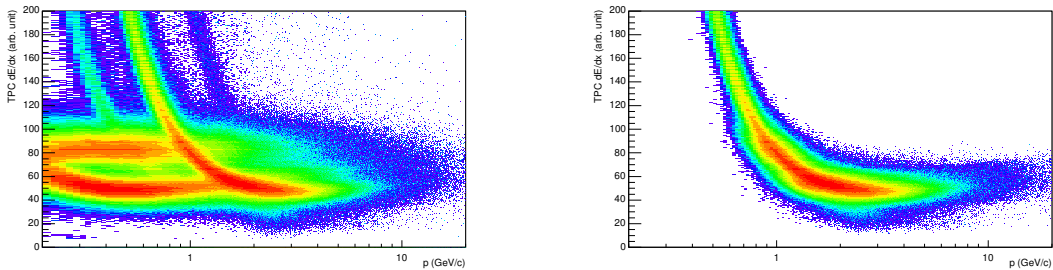


Figure 23: TPC dE/dx as function of transverse momentum for total (top) and selected proton in 3σ (bottom)

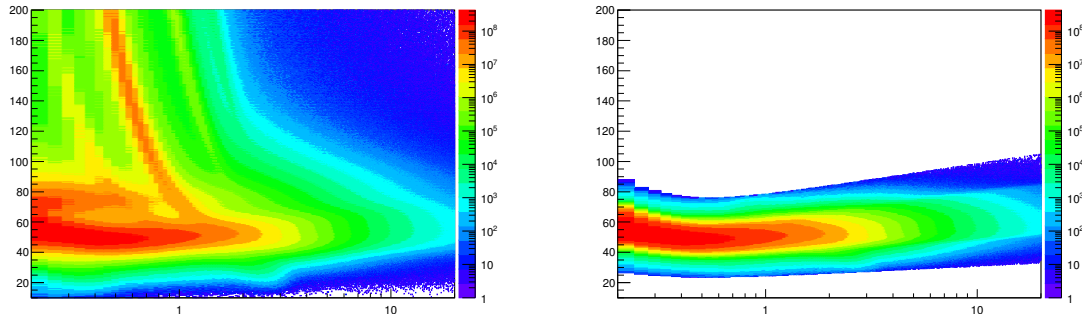


Figure 24: TPC dE/dx as function of transverse momentum for total (top) and selected first emitted π in 3σ (bottom)

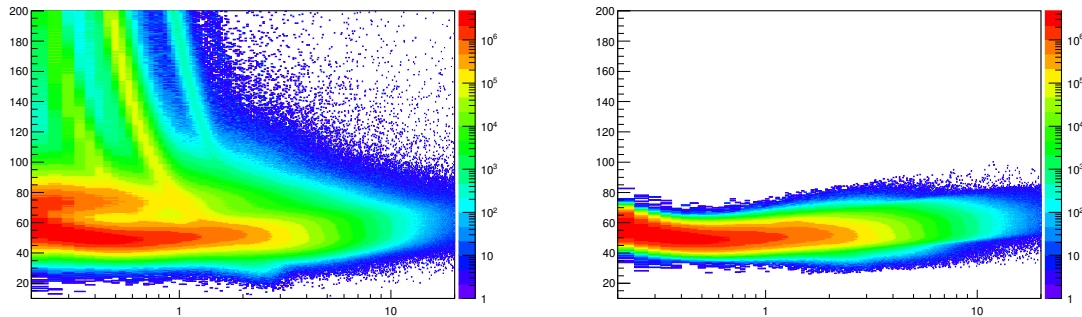


Figure 25: TPC dE/dx as function of transverse momentum for total (top) and selected second emitted π in 3σ (bottom)

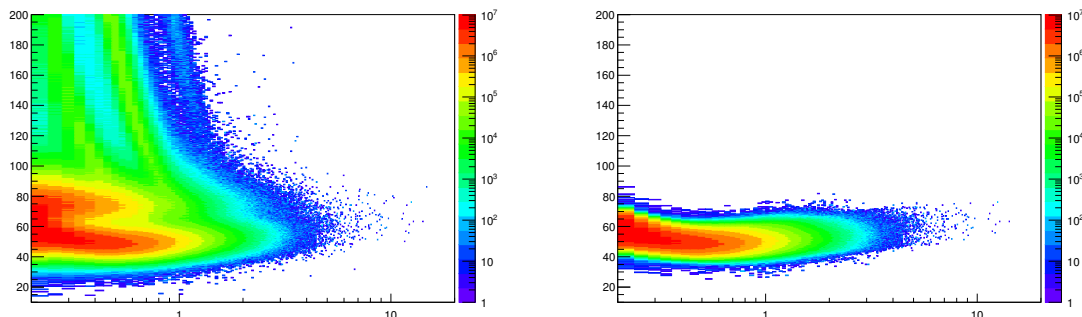


Figure 26: TPC dE/dx as function of transverse momentum for total (top) and selected last emitted π in 3σ (bottom)

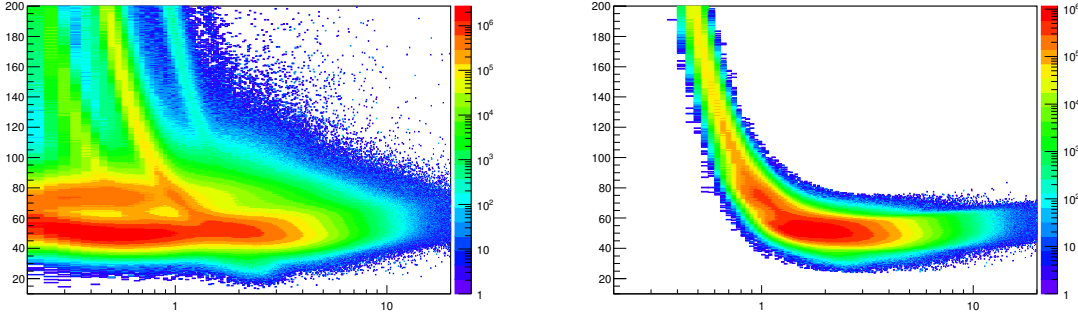


Figure 27: TPC dE/dx as function of transverse momentum for total (top) and selected proton in 3σ (bottom)

908 **5.1.4 Signal extraction**

909 The Ξ^{*0} signals were reconstructed by invariant-mass analysis of candidates for the decay
 910 products in each transverse momentum interval of the resonance particle, and for each
 911 multiplicity class. The $\Xi^-\pi^+(\Xi^+\pi^-)$ invariant mass distribution is reported in Figure 5.1.4
 912 for semi-central events (20-40%) in p-Pb collisions and Figure 5.1.4 for central events(0-
 913 10%) in Pb-Pb collisions.

914 Since the resonance decay products originate from a position which is indistinguishable
 915 from the PV, a significant combinatorial background is present. In order to extract
 916 $\Xi(1530)^0$ signal it is necessary to remove or, at least reduce, the combinatorial background.
 917 For this analysis, this has been done with the event mixing (EM) technique, by combining
 918 uncorrelated decay products 20 different events in p-Pb (5 different events in Pb-Pb). The
 919 events for the mixing have been selected by applying the similarity criteria to minimise
 920 distortions due to different acceptances and to ensure a similar event structure, only tracks
 921 from events with similar vertex positions z ($|\Delta z| < 1$ cm) and track multiplicities n ($|\Delta n| <$
 922 10) were taken.

923 The mixed-event background distributions were normalised to two fixed regions,
 924 $1.49 < M_{\Xi\pi} < 1.51$ GeV/c^2 and $1.56 < M_{\Xi\pi} < 1.58$ GeV/c^2 , around the Ξ^{*0} mass
 925 peak (Figure 5.1.4 and 5.1.4). These regions were used for all p_T intervals and multiplicity
 926 classes, because the background shape is reasonably well reproduced in these regions and
 927 the invariant-mass resolution of the reconstructed peaks appears stable, independently of
 928 p_T . The uncertainty on the normalisation was estimated by varying the normalisation
 929 regions and is included in the quoted systematic uncertainty for the signal extraction (Section 5.4).

931 After the background subtraction, the resulting distribution is shown in Figure 5.1.4
 932 and 5.1.4. In order to obtain raw yields, a combined fit of a first-order polynomial for

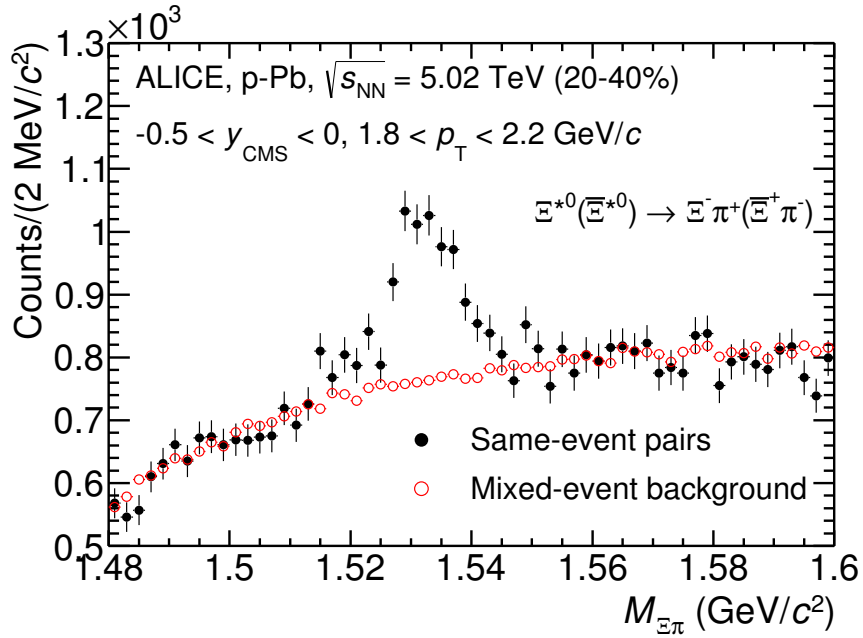


Figure 28: The $\Xi^\pm\pi^\pm$ invariant mass distribution (Same-event pairs) in $1.8 < p_T < 2.2$ GeV/c and for the multiplicity class 20-40%. The background shape, using pairs from different events (Mixed-event background), is normalised to the counts in $1.49 < M_{\Xi\pi} < 1.51$ GeV/c 2 and $1.56 < M_{\Xi\pi} < 1.58$ GeV/c 2 .

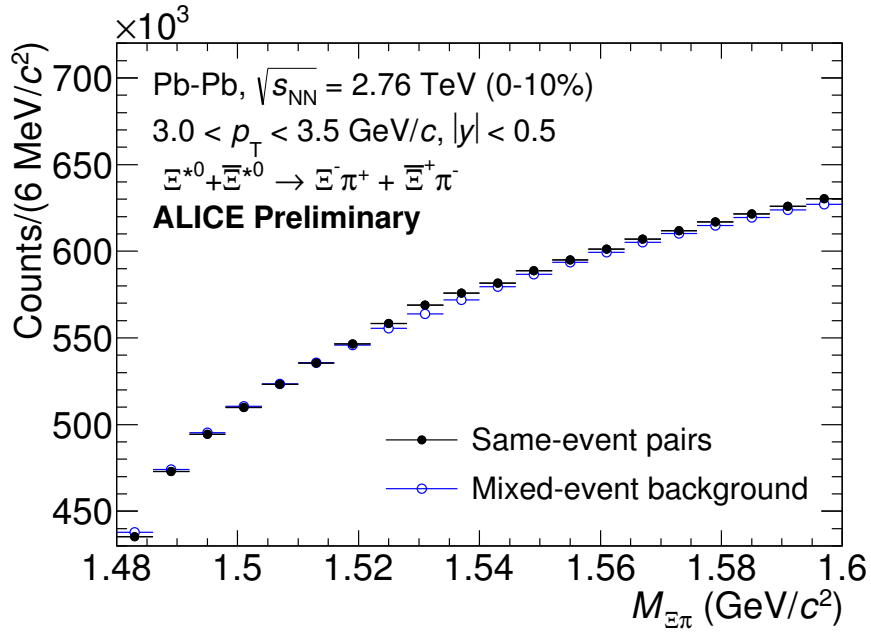


Figure 29: The $\Xi^\pm\pi^\pm$ invariant mass distribution (Same-event pairs) in $3.0 < p_T < 3.5$ GeV/c and for the centrality class 0-10%. The background shape, using pairs from different events (Mixed-event background), is normalised to the counts in $1.49 < M_{\Xi\pi} < 1.51$ GeV/c² and $1.56 < M_{\Xi\pi} < 1.58$ GeV/c².

933 the residual background and a Voigtian function (a convolution of a Breit-Wigner and a
 934 Gaussian function accounting for the detector resolution) for the signal was used. The
 935 mathematical form of fit function used in analysis is:

$$f(M_{\Xi\pi}) = \frac{Y}{2\pi} \frac{\Gamma_0}{(M_{\Xi\pi} - M_0)^2 + \frac{\Gamma_0^2}{4}} \frac{e^{-(M_{\Xi\pi} - M_0)/2\sigma^2}}{\sigma\sqrt{2\pi}} + bg(M_{\Xi\pi}) \quad (7)$$

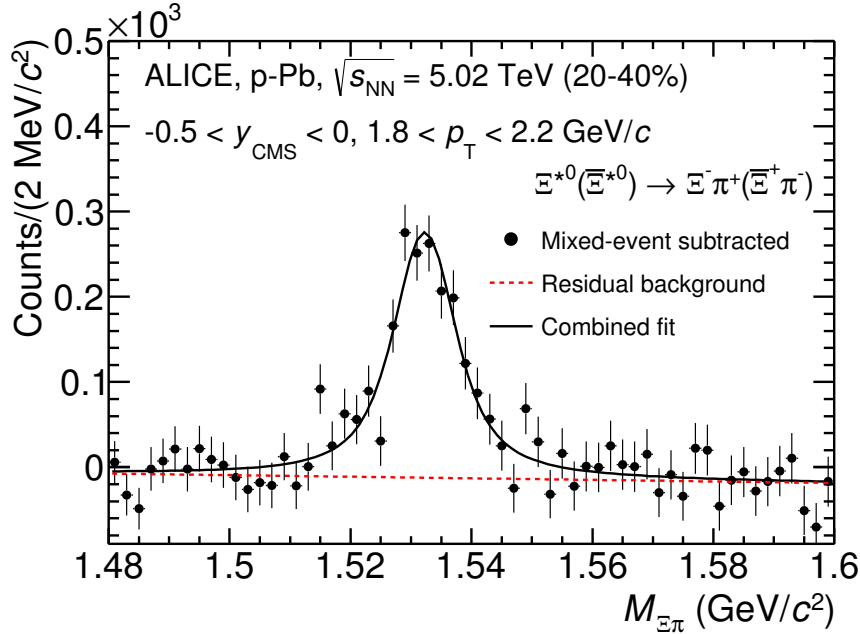


Figure 30: The invariant mass distribution after subtraction of the mixed-event background in p–Pb collisions. The solid curve represents the combined fit, while the dashed line describes the residual background.

936 The mass parameter of the Voigtian fit (M_0) is left free within the fit range ($1.48 \text{ GeV}/c^2$
 937 and $1.59 \text{ GeV}/c^2$). The overall invariant mass width of the Voigtian function is governed
 938 by 2 parameters: σ and Γ_0 . The σ describes the broadening of the peak due to finite
 939 detector resolution while Γ describes the intrinsic width of the resonance itself. The Γ_0 is
 940 fixed to the PDG value of $9.1 \text{ MeV}/c$ for the $\Xi(1530)^0$. Because of lack of statistics, the
 941 σ can be over estimated. Therefore the σ parameter is fixed to value derived from σ in
 942 MB events which has largest statistics. The σ as function of p_T distribution in MB events
 943 is shown in Figure. 32 and we also report invariant mass of $\Xi(1530)^0$ as function of p_T in
 944 Figure. 33. The $\Xi(1530)^0$ raw yields have been extracted from the fit for the 4 multiplicity

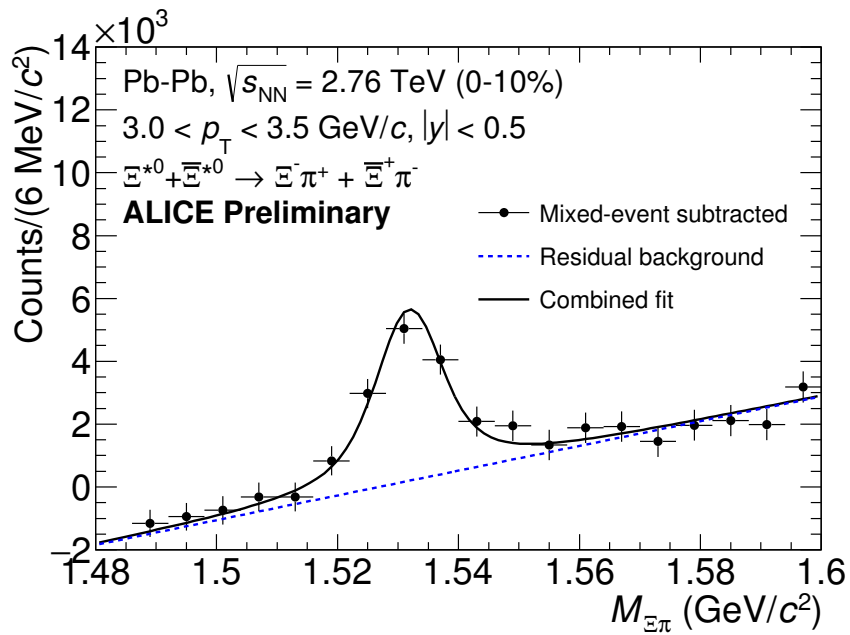


Figure 31: The invariant mass distribution after subtraction of the mixed-event background in Pb–Pb collisions. The solid curve represents the combined fit, while the dashed line describes the residual background.

⁹⁴⁵ bins (+ NSD events) in p–Pb and 4 centrality bins in Pb–Pb collisions and the yields as
⁹⁴⁶ function of p_T are shown in Figure 34.

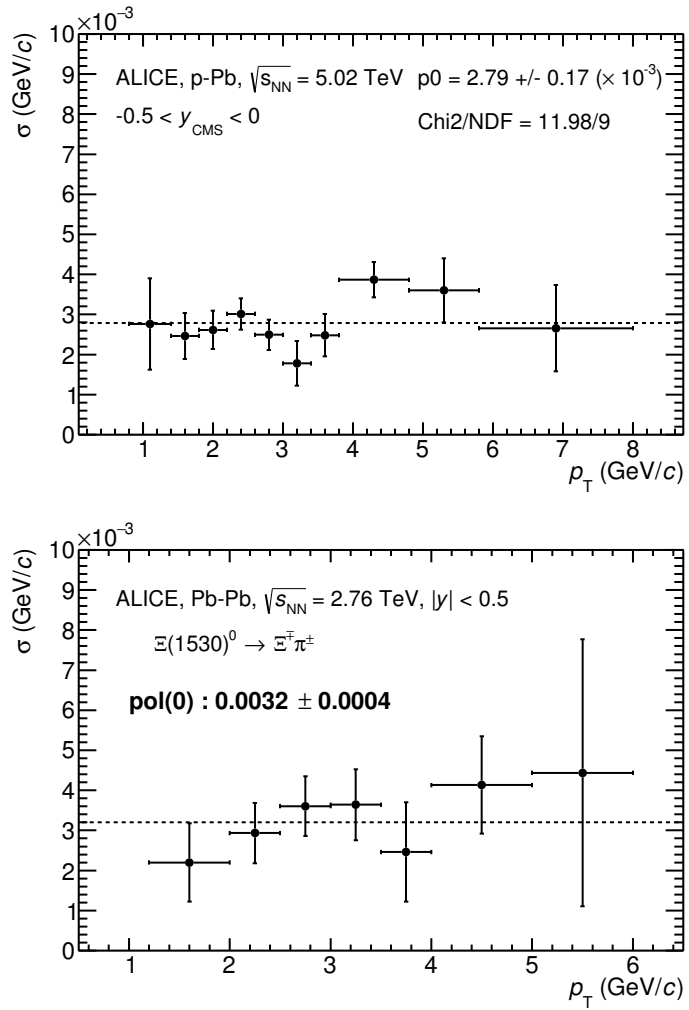


Figure 32: σ fit parameters as a function of p_T in MB in p-Pb collisions (top) and in Pb-Pb collisions (bottom).

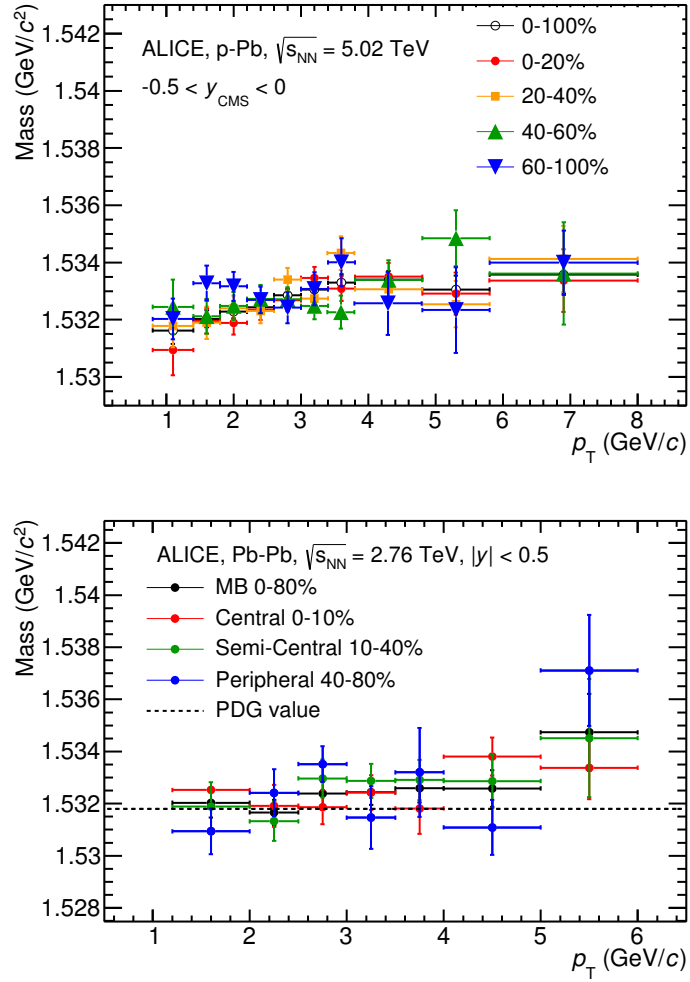


Figure 33: $\Xi(1530)^0$ -mass obtained from fit of the Voigtian peak as a function of p_T in each multiplicity classes in p-Pb collisions (top) and the different centrality classes in Pb-Pb (bottom).

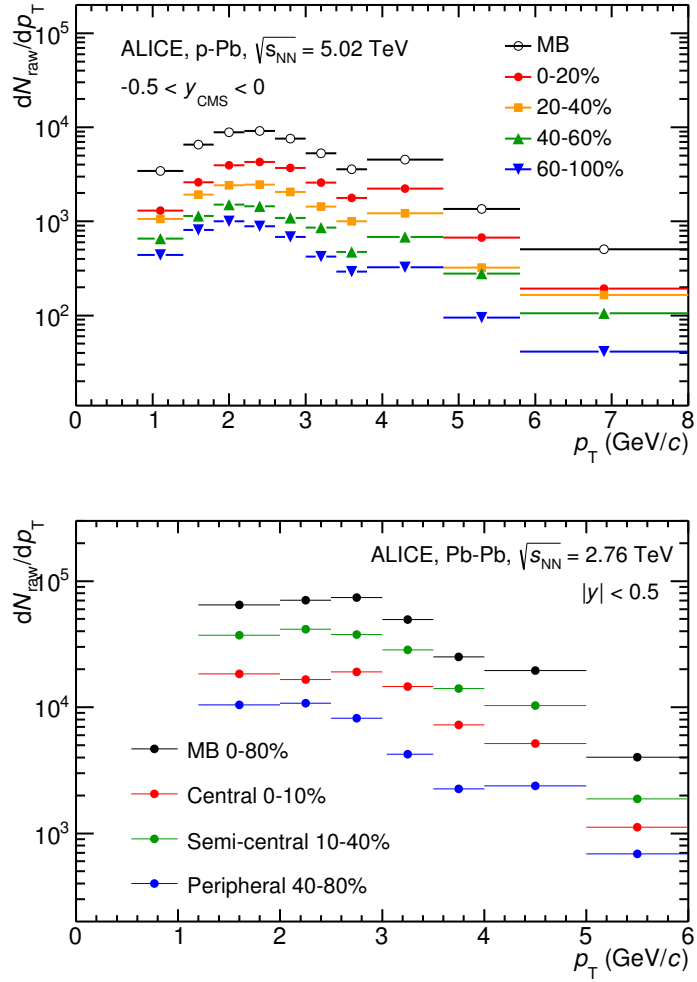


Figure 34: $\Xi(1530)^0$ -raw spectra obtained from fit of the Voigtian peak and a polynomial residual background for different multiplicities in p-Pb collisions (top) and Pb-Pb collisions (bottom). Only the statistical error is reported.

947 **5.2 Efficiency correction**

948 The raw yields were corrected for the geometrical acceptance and the reconstruction effi-
 949 ciency ($A \times \epsilon$) of the detector (Figure. 35). By using the DPMJET 3.05 event generator [37]
 950 and the GEANT 3.21 package [38], a sample of about 100 million p–Pb events was sim-
 951 ulated and reconstructed in order to compute the corrections. The distributions of $A \times \epsilon$
 952 were obtained from the ratio between the number of reconstructed Ξ^{*0} and the number of
 953 generated particle in the same p_T and rapidity interval. Since the correction factors for
 954 different multiplicity classes are in agreement with those from MB events within statistical
 955 uncertainty, the latter were used for all multiplicity classes.

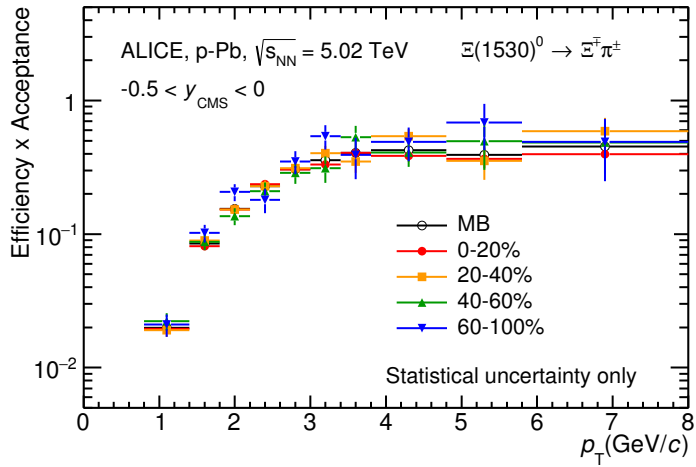


Figure 35: $\Xi(1530)^0$ -raw spectra obtained from fit of the Voigtian peak and a polynomial residual background for different multiplicities. Only the statistical error is reported.

956 Because the generated $\Xi(1530)^0$ spectra have different shapes than the measured $\Xi(1530)^0$
 957 spectra, it is necessary to weight the generated and reconstructed $\Xi(1530)^0$ spectra in these
 958 simulations. Fig. 36 shows the generated and reconstructed $\Xi(1530)^0$ spectra plotted with
 959 the (corrected) measured $\Xi(1530)^0$ spectrum for MB events and the Levy fit of that mea-
 960 sured spectrum. The generated and measured $\Xi(1530)^0$ spectra have different behaviours
 961 for the range $0.5 < p_T < 1$ GeV/c . The generated $\Xi(1530)^0$ spectrum decreases with
 962 increasing p_T over this range, while the fit of the measured $\Xi(1530)^0$ spectrum reaches a
 963 local maximum in this range. The correction ϵ is observed to change rapidly over this
 964 p_T range. It is therefore necessary to weight the generated spectrum so that it has the
 965 shape of the measured $\Xi(1530)^0$ spectrum (and to apply corresponding weights to the re-
 966 constructed $\Xi(1530)^0$ spectrum). An iterative procedure is performed to determine the
 967 correct weighting (and therefore the correct ϵ).

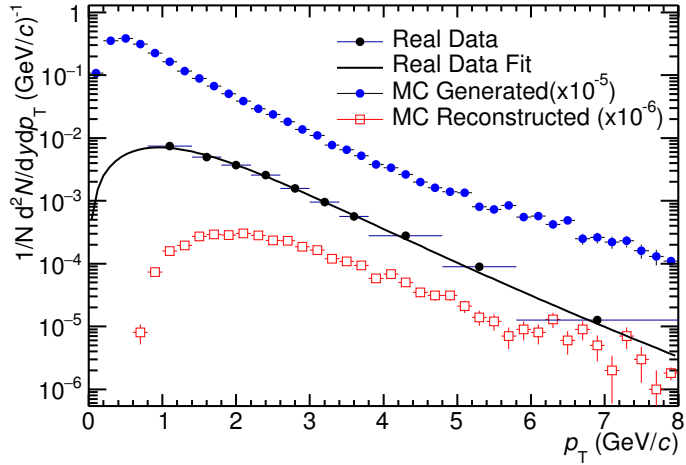


Figure 36: Real corrected $\Xi(1530)^0$ spectrum (black) for the minimum bias with Levy fit (black curve). Also shown are the unweighted generated (blue) and reconstructed (red) $\Xi(1530)^0$ spectra.

- 968 1. The unweighted ϵ is calculated.
 969 2. This ϵ is used to correct the measured xis spectrum.
 970 3. The corrected $\Xi(1530)^0$ spectrum is fit.
 971 4. This fit is used to weight the simulated xis spectra. A p_T dependent weight is applied
 972 to the generated xis spectrum so that it follows the fit. The same weight is applied
 973 to the reconstructed xis spectrum.
 974 5. The (weighted) ϵ is calculated.
 975 6. Steps 2-5 are repeated (with the weighted ϵ from step 5 used as the input for step 2)
 976 until the ϵ values are observed to change by $< 0.1\%$ (relative) between iterations. It
 977 is observed that four iterations are sufficient for this procedure to converge.

978 Finally, the re-weighted efficiency is obtained and the distribution as function of p_T is
 979 shown in Figure 37.

980 In order to obtain the correction factor dedicated in Pb-Pb collisions, MC events are
 981 generated using Heavy Ion Jet Interaction Generator (HIJING). The generated events are
 982 passed through a GEANT3 model of the ALICE experiment with a realistic description of
 983 the detector response. Because we have observed centrality dependent efficiency, the cen-
 984 trality dependent efficiencies have been applied to get corrected raw yield. The reweighting

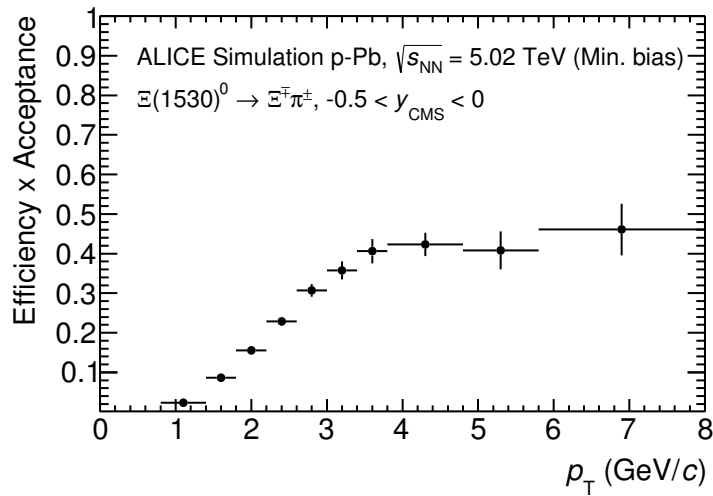


Figure 37: Efficiency as a function of p_T in minimum bias events in p-Pb collisions.

985 approach which was used to correct the efficiency in p-Pb is also applied to the efficiency
 986 obtained in Pb-Pb.

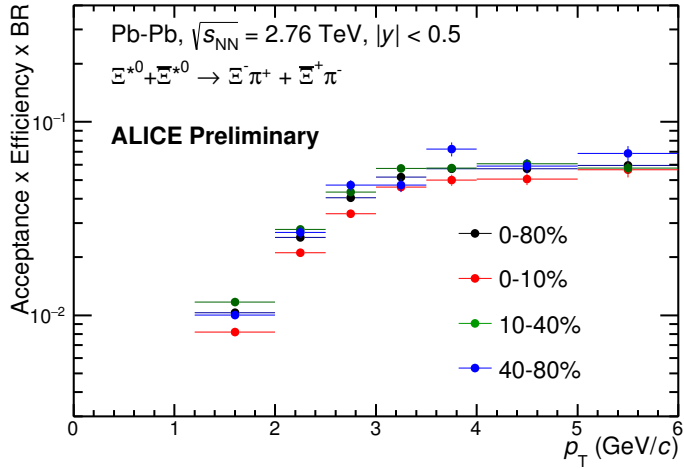


Figure 38: Efficiency as a function of p_T in different centrality classes in Pb–Pb collisions

987 **5.3 Corrected p_T -spectra**

988 The p_T spectrum is by the number of produced particles of a given type in the desired
 989 interval of phase-space divided by the number of inelastic collisions. The spectrum is
 990 calculated as:

$$\frac{1}{N} \times \frac{d^2N}{dydp_T} = \frac{1}{N_{E,PhysSel}} \times \frac{N_{raw}}{dp_T dy} \frac{1}{\epsilon} \frac{N_{total}^{MC}}{N_{post-PVcut}^{MC}}, \quad (8)$$

991 where N_E represent the number inelastic collisions, the $\frac{dN}{dydp_T}$ is the yield per range of
 992 rapidity y , per range in p_T . On the right hand side $N_{E,PhysSel}$ is the number of events
 993 counted by the physics selection trigger. N_{raw} is the raw extracted number of particle in the
 994 rapidity and p_T bin of width $\Delta y = 0.5$ in p–Pb ($\Delta y = 1.0$ in Pb–Pb) and Δp_T , respectively.
 995 ϵ is the reconstruction efficiency estimated from Monte Carlo simulations. $\frac{N_{total}^{MC}}{N_{post-PVcut}^{MC}}$ is the
 996 ratio of the total number of particle from MC divided by the number of particle from MC
 997 after the Primary-Vertex cut is imposed. It takes into account the fraction of particle lost
 998 after imposing the PV cut. We notice that for minimum-bias results in p–Pb, we adopted
 999 a normalisation such that to provide result from non-single diffractive(NSD) cross-section.
 1000 The normalisation factor is 0.964 [5]. The obtained spectrum at MB and the spectrums
 1001 from different multiplicity classes in p–Pb are shown in Figure 39 and different centrality
 1002 classes in Pb–Pb are shown in Figure 40.

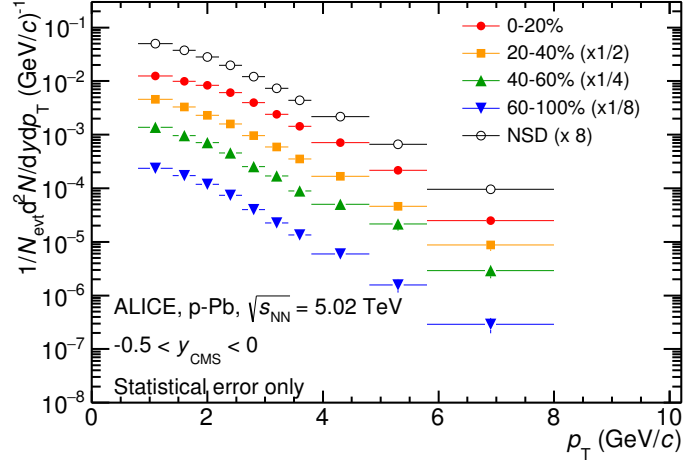


Figure 39: Corrected p_T -spectra of $\Xi(1530)^0$ in NSD and different multiplicity classes in p-Pb collisions.

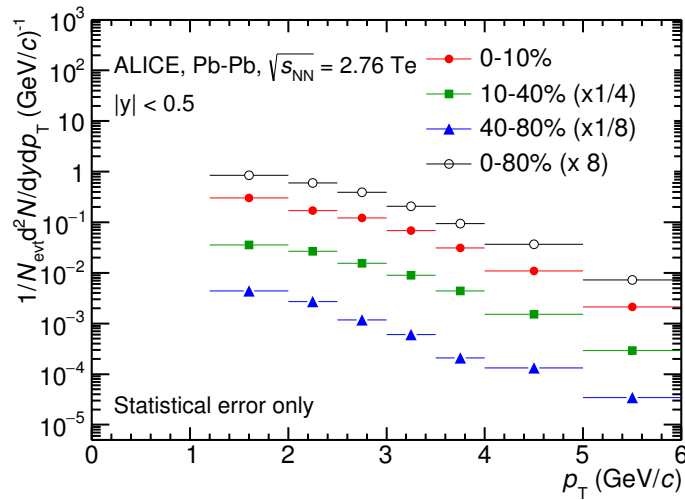


Figure 40: Corrected p_T -spectra of $\Xi(1530)^0$ in different centrality classes in Pb-Pb collisions.

1003 **5.4 Systematic uncertainties**

1004 The systematic uncertainties are calculated in seven principle groups. The procedure to ob-
1005 tain the systematic uncertainties is performed many times by varying the possible permuta-
1006 tion of the analysis parameter. The general strategy for evaluating systematic uncertainties
1007 is described as following:

- 1008 1. Choose one set of parameters for the analysis as default
1009 2. Observe the deviation of yield when one parameter is changed
1010 3. The systematic uncertainty is calculated for a given source as the RMS deviation of
1011 the available sources.
1012 4. The total systematic uncertainty, taking into account all the different sources, is the
1013 sum in quadrature of each source.

1014 To study the systematic effect we repeat the measurement by varying one parameter at
1015 a time. A Barlow [39] check has been performed for each measurement to verify whether it
1016 is due to a systematic effect or a statistical fluctuation. Let each measurement be indicated
1017 by $(y_i \pm \sigma_i)$ and the central value (default measurement) by $(y_c \pm \sigma_c)$, one can define $\Delta\sigma_i$
1018 (Eq. 9).

$$\Delta\sigma_i = \sqrt{(|\sigma_i^2 - \sigma_c^2|)} \quad (9)$$

1019 Then we calculate $n_i = \Delta y_i / \Delta\sigma_i$, where $\Delta y_i = |y_c - y_i|$. If $n_i \leq 1.0$ then the effects
1020 are due to the statistical fluctuation and if $n_i > 1.0$ we apply consistency check. Since
1021 the alternate and default measurements are not statistically independent, an alternate
1022 measurement which is statistically consistent with the default measurement should not be
1023 used in calculating a systematic uncertainty. The difference between the two measurements
1024 is $\Delta = y_c - y_i$. The difference in quadrature of the uncertainties is calculated by Eq. 9. It
1025 could be possible to check if $\Delta < \sigma$ and exclude such cases from the systematic uncertainties.
1026 However, there can be statistical fluctuations for which $\Delta > \sigma$. If the variations between the
1027 default and alternate measurements are purely statistical, the distribution of Δ/σ should
1028 be a Gaussian with a mean value that is consistent with zero and a deviation σ consistent
1029 with unity. In this analysis, if the mean value is less than 0.1 and σ is less than 1, the
1030 variation passes the consistency check.

1031 Only the measurements which passed the Barlow check ($n_i > 1$) are used to determine
1032 the systematic uncertainty. For measurements $N > 2$, the systematic uncertainty has been
1033 determined as the RMS (eqn. 10) of the available measurements. If $N=2$, the absolute
1034 difference is assigned as systematic uncertainty.

$$\delta y_{syst.} = \sqrt{\frac{1}{N} \sum_i (y_i - \bar{y})^2} \quad (10)$$

1035 Here N is the total number of available measurements including y_c and \bar{y} is the average
1036 of value of the measurements. The measurement did not pass Barlow check, zero systematic
1037 uncertainty has been assigned to the value.

1038 By suing the way as explained above, all the main contributions to the systematic un-
1039 certainty of particle spectra have been studied. In particular those that comes from signal
1040 extraction, topological and kinematical selection cuts, track quality selection and $n\sigma$ TPC
1041 PID variation. the meaning of each source of systematic uncertainty studied is described
1042 in the following:

1043

1044 **Signal extraction**

1045 We have extracted the signal with varying the yield calculating method which contains
1046 the method of signal extraction by integrating the Voigtian fit function and bin counting.
1047 We also have varied the normalisation range which is related to the invariant mass region
1048 where the mixed events distribution is scaled to subtract the combinatorial background
1049 and different background estimator such as Like-Sign distribution and polynomial fit was
1050 taken account into the systematic source of signal extraction. The systematic uncertainty
1051 from signal extraction is sum in quadrature of three sources.

1052

1053 **Topological selection**

1054 To evaluate the stability of the chosen set of values for the topological cuts, loose and tight
1055 cuts have beed defined in order to vary by $\pm 10\%$ respectively. The parameters are changed
1056 once at a time. Total systematic uncertainty from topological selection is calculated by
1057 summation in quadrature of nine sources.

1058

1059 **TPC $N_{cluster}$ selection**

1060 The selection performed for the daughter tracks of the cascade is that $N_{cluster}$ is larger
1061 than 70 and the value has been varied to 60 and 80 in order to estimate the systematic
1062 uncertainty due to this selection.

1063

1064 **TPC dE/dx selection**

1065 In order to evaluate any potential effect due to the TPC dE/dx selection (U_{PID}), the N_σ
1066 selection was varied with $N = 2.5$ and 3.5 .

1067

1068 **p_T shape correction**

1069 As described in Section 5.2, due to the different shape of the measured and generated
1070 $\Xi(1530)^0$ spectra, we have applied reweighing procedure to the generated spectra to have
1071 same shape and this correction is added into contributor of systematic uncertainty as
1072 p_T shape correction.

1073

1074 **Mass window range selection**

1075 In order to select Ξ^\pm which is daughter particle of $\Xi(1530)^0$, we apply the mass window

1076 ± 7 MeV/ c^2 around $\Xi(1530)^0$ mass on $\Lambda\pi$ invariant mass distribution. The boundaries
1077 has been varied to ± 6 MeV/ c^2 and ± 8 MeV/ c^2 to estimate systematic uncertainty.

1078

1079 **Vertex range selection**

1080 The distribution of vertex-z is shown in Fig.16. The cut on $|Vz|$ was varied from the nominal
1081 ± 10 cm to ± 9 cm, ± 11 cm.

1082

1083 **Material Budget and hadronic cross section**

1084 A possible source of uncertainty comes from the description of the material, active (detecting
1085 area) or dead (structure and cable), that the particles cross during their travel in
1086 the MC with respect to the real material present in the detector. Such description could
1087 affect the reconstruction efficiency in different aspects (e.g. multiple scattering, energy
1088 loss). The value estimated by Ξ analysis [40] has been used in this study which gives 4%
1089 systematic uncertainty. In case of systematic uncertainty from hadronic cross section, we
1090 have inherited the value studied in previous measurement[41] which amount is 1%.

1091

1092 **Tracking efficiency**

1093 Systematic uncertainties from tracking efficiency from ITS + TPC combined track were
1094 assigned as 3% in p–Pb and 4% in Pb–Pb collision system.[41]

1095 (<https://twiki.cern.ch/twiki/bin/view/ALICE/TrackingEfficiencyCharged>)

1096

1097 Finally, total systematic uncertainty is sum in quadrature of sources listed above. Figure
1098 41 and Figure 42 show the total systematic uncertainty in minimum bias event and
1099 different multiplicity classes in p–Pb collisions, respectively. Again, Figure 43 and Figure
1100 44 present the total systematic uncertainty in minimum bias event and different centrality
1101 classes in Pb–Pb collisions.

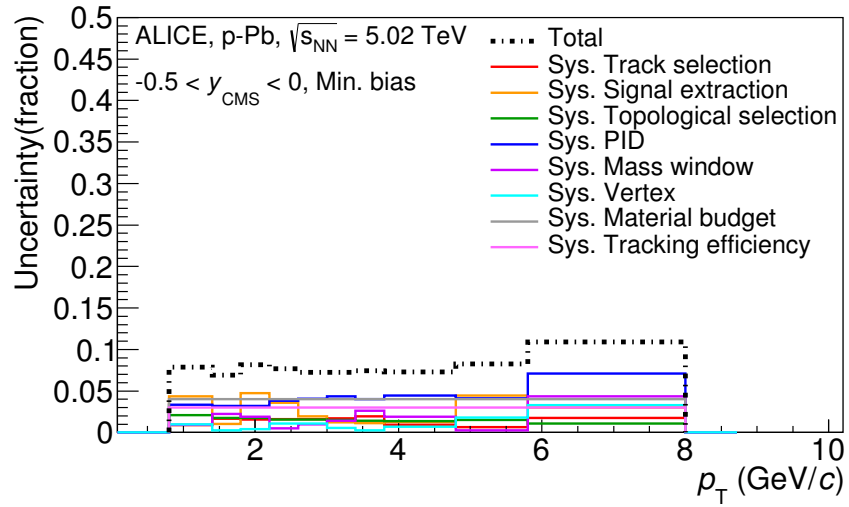


Figure 41: Summary of the contributions to the systematic uncertainty in minimum bias events in p–Pb collisions. The dashed black line is the sum in quadrature of all the contributions.

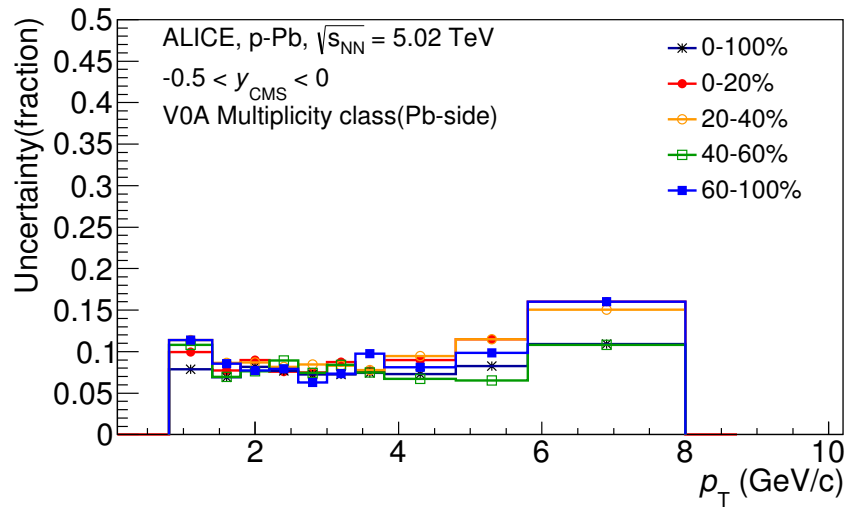


Figure 42: Systematic uncertainties for each multiplicity classes in p–Pb collisions.

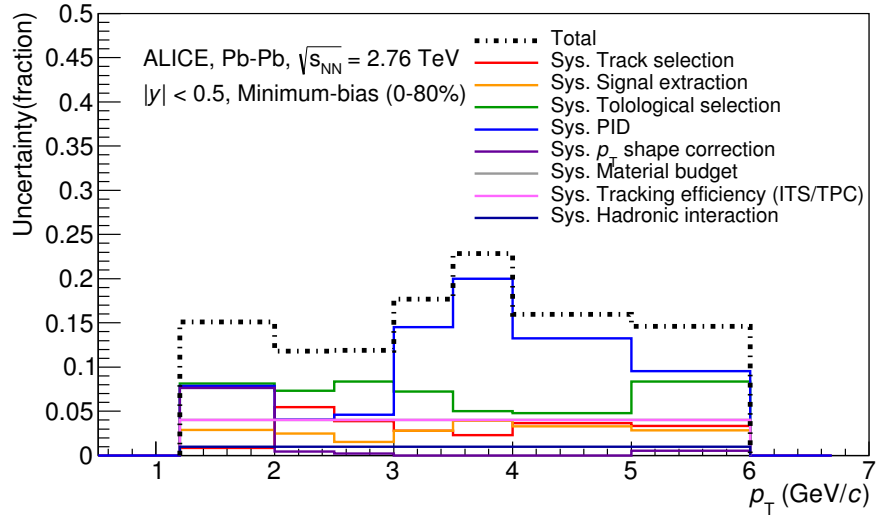


Figure 43: Summary of the contributions to the systematic uncertainty in minimum bias events in Pb–Pb collisions. The dashed black line is the sum in quadrature of all the contributions.

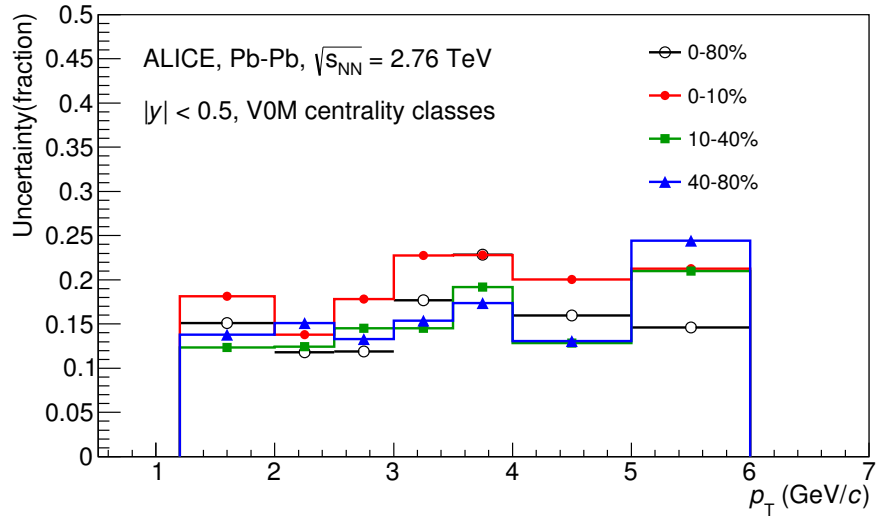


Figure 44: Systematic uncertainties for each multiplicity classes.

Source of uncertainty	p-Pb	Pb-Pb
<i>p</i> _T -dependent		
Tracking efficiency	3%	4%
Tracks selection	1-2%	1-5%
Topological selection	1-2%	5-8%
PID	3-7%	4-20%
Signal extraction	1-5%	1-4%
<i>p</i> _T shape correction	-	0-8%
Mass window (Ξ^\pm)	4%	-
Vertex selection	3%	-
<i>p</i> _T -independent		
Hadronic interaction	-	1%
Material budget	4%	4%
Branching ratio	0.3%	0.3%
Total	8-12%	9-25 %

Table 8: Summary of the systematic uncertainties on the differential yield, $d^2N/(dp_T dy)$. Minimum and maximum values in all p_T intervals and multiplicity classes in p–Pb, centrality classes in Pb–Pb are shown for each source.

1102 **5.5 $\Xi(1530)^0$ transverse momentum spectra**

1103 The raw yield shown in Figure 39 and 40 have been corrected for efficiency as described
 1104 in section 5.2. The measured spectra for $(\Xi(1530)^0 + \bar{\Xi}(1530)^0)/2$ are reported in Figure
 1105 45 for p–Pb collisions and Figure 46 for Pb–Pb collisions. The statistical and systematic
 1106 uncertainties are reported respectively as the error bars and the boxes on the plot. The
 1107 corrected yields for p–Pb collisions are measured with $0.8 < p_T < 8.0$ GeV/c while the
 1108 yields for Pb–Pb collisions are obtained with $1.2 < p_T < 6.0$ GeV/c due to difficulty of
 1109 signal extraction in low and high p_T region.

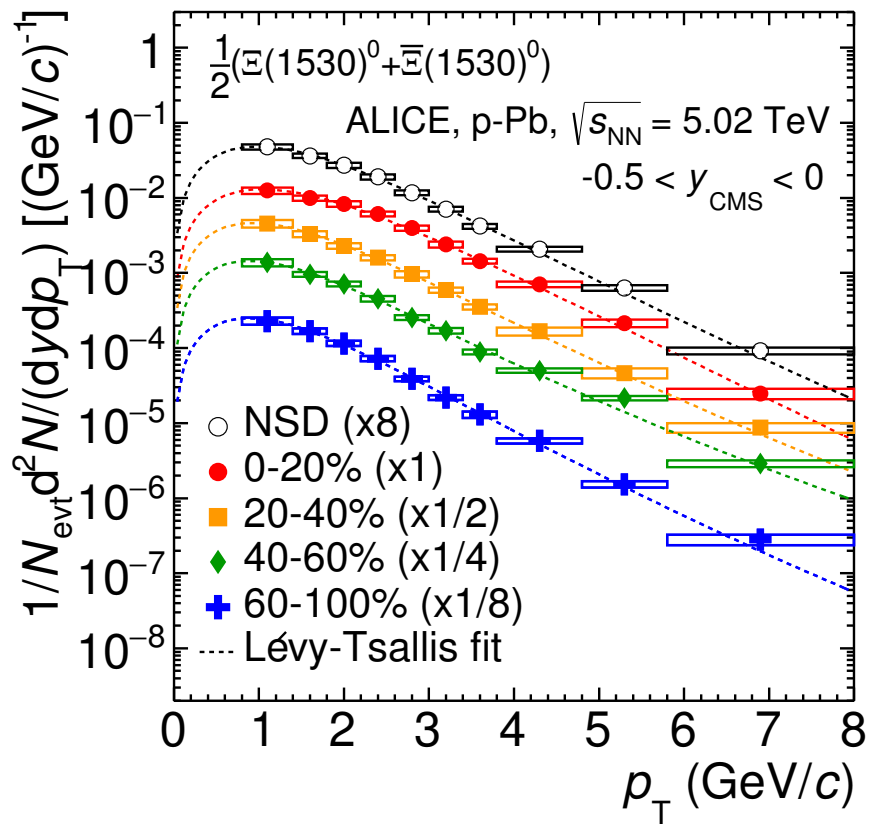


Figure 45: Corrected yields as function of p_T in NSD events and multiplicity dependent event classes in p-Pb collision system. Statistical uncertainties are presented as bar and systematical uncertainties are plotted as boxes.

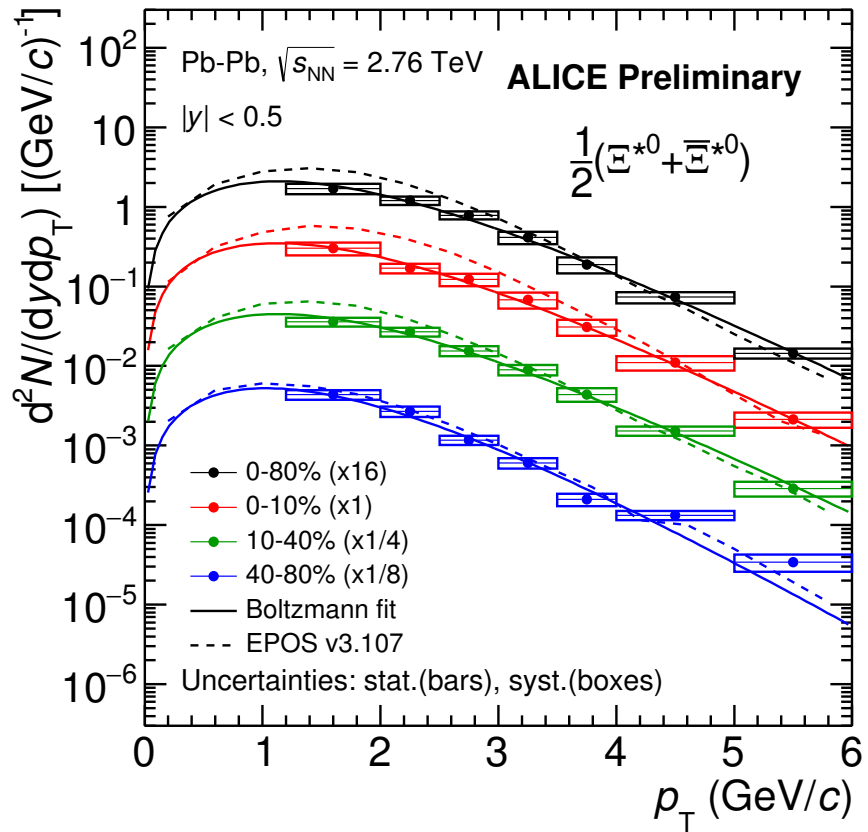


Figure 46: Corrected yields as function of p_T in different centrality classes in Pb–Pb collision system. Statistical uncertainties are presented as bar and systematical uncertainties are plotted as boxes.

1110 **6 Further results and discussion**

1111 The transverse momentum distributions of double-strange hyperon resonances, $\Xi(1530)^0$
1112 , produced in p–Pb collisions at $\sqrt{s_{\text{NN}}}= 5.02$ TeV and Pb–Pb collisions at $\sqrt{s_{\text{NN}}}= 2.76$
1113 TeV were measured in the mid-rapidity range and they have been already presented in
1114 Chapter 5. From the measurement, the $\langle p_{\text{T}} \rangle$ and integrated particle yield ratios with
1115 system size have been obtained. In the present Chapter these results are compared with
1116 model predictions and discussed in connection with the following topics:

- 1117
 - Mean transverse momentum studies
 - Study of particle production mechanism in hadronic phase
 - Study of strangeness enhancement

1120 Most of the theoretical aspects related to these topics and, in particular, the description
1121 of the models already have been addressed in Chapter 3.

1122 **6.1 Mean transverse momentum**

1123 Figure 47 shows the mean transverse momentum $\langle p_{\text{T}} \rangle$ as a function of mean charged-
1124 particle multiplicity density $\langle dN_{\text{ch}}/d\eta_{\text{lab}} \rangle$ at midrapidity. The results for $\Xi(1530)^0$ are
1125 compared with those for other hyperons observed in p–Pb collisions at $\sqrt{s_{\text{NN}}}= 5.02$ TeV [4,
1126 6].

1127 Increasing trends from low to high multiplicities are observed for all hyperons. The
1128 mean transverse momenta increase by 20% as the mean charged-particle multiplicity in-
1129 creases from 7.1 to 35.6. This result is similar to the one obtained for the other hyperons.
1130 Furthermore, a similar increase has been observed also for K^{\pm} , K_S^0 , $K^*(892)^0$ and ϕ [5],
1131 whereas protons are subject to a larger ($\sim 33\%$) increase in the given multiplicity range,
1132 as discussed also in Ref. [4].

1133 In all multiplicity classes, the $\langle p_{\text{T}} \rangle$ follows an approximate mass ordering:

- 1134
 - $\langle p_{\text{T}} \rangle_{\Lambda} < \langle p_{\text{T}} \rangle_{\Xi^-} \simeq \langle p_{\text{T}} \rangle_{\Sigma^{*\pm}} < \langle p_{\text{T}} \rangle_{\Xi^{*0}} < \langle p_{\text{T}} \rangle_{\Omega^-}$

1135 The $\langle p_{\text{T}} \rangle$ of $\Sigma^{*\pm}$ looks systematically lower than the $\langle p_{\text{T}} \rangle$ of Ξ^- , despite the larger mass
1136 of $\Sigma^{*\pm}$. The uncertainties, however, are too large to draw any conclusion on possible hints
1137 of violation of the mass hierarchy. This hierarchy of mass-ordering, also including D^0 and
1138 J/ψ in the comparison, is displayed in Figure 48. Note, however, that the D^0 and J/ψ
1139 were measured in different rapidity ranges: $|y_{\text{CMS}}| < 0.5$ [8] ($|y_{\text{CMS}}| < 0.9$ [9]) for D^0 (J/ψ)
1140 in pp and $-0.96 < y_{\text{CMS}} < 0.04$ [8] ($-1.37 < y_{\text{CMS}} < 0.43$ [10]) for D^0 (J/ψ) in p–Pb, and
1141 the results for D^0 and J/ψ in p–Pb collisions are for the 0–100% multiplicity class. This
1142 mass dependence is observed in both p–Pb and pp collisions. It was observed also by the
1143 STAR collaboration [42] in MB pp, MB d–Au and central Au–Au collisions.

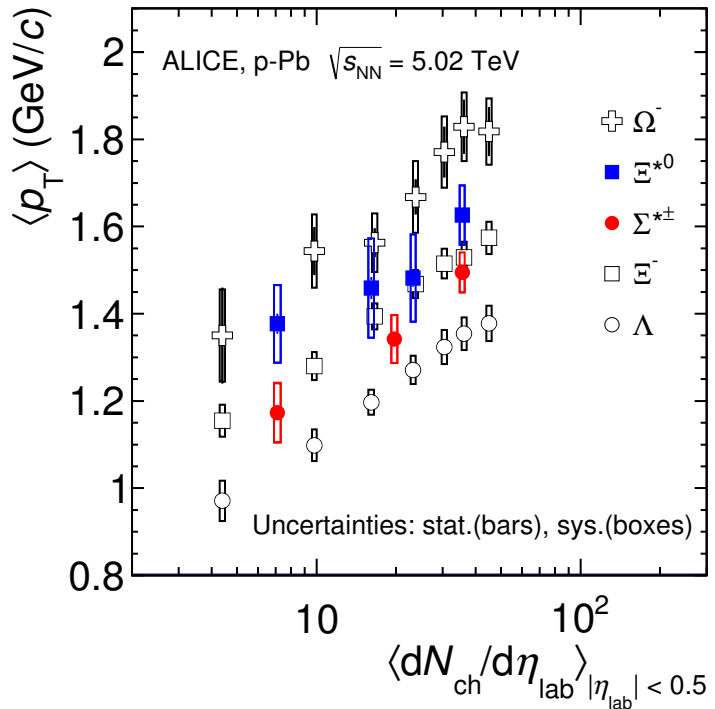


Figure 47: Mean transverse momenta $\langle p_T \rangle$ of Λ , Ξ^- , $\Sigma^{*\pm}$, Ξ^{*0} and Ω^- in p-Pb collisions at $\sqrt{s_{NN}} = 5.02$ TeV as a function of mean charged-particle multiplicity density $\langle dN_{ch}/d\eta_{lab} \rangle$, measured in the pseudorapidity range $|\eta_{lab}| < 0.5$. The results for Λ , Ξ^- and Ω^- are taken from [4, 5, 6]. Statistical and systematic uncertainties are represented as bars and boxes, respectively. The Ω^- and Ξ^- points in the 3rd and 4th lowest multiplicity bins are slightly displaced along the abscissa to avoid superposition with the $\Xi(1530)^0$ points.

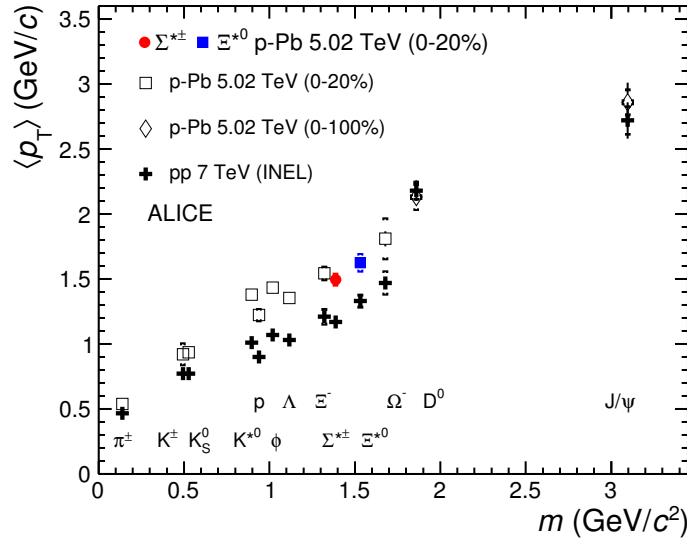


Figure 48: Mass dependence of the mean transverse momenta of identified particles for the 0 – 20% V0A multiplicity class and with $-0.5 < y_{\text{CMS}} < 0$ in p–Pb collisions at $\sqrt{s_{\text{NN}}}=5.02$ TeV [4, 6], and in minimum-bias pp collisions at $\sqrt{s}=7$ TeV [7] with $|y_{\text{CMS}}| < 0.5$. Additionally, D^0 and J/ψ results are plotted. The D^0 and J/ψ were measured in different rapidity ranges: $|y_{\text{CMS}}| < 0.5$ [8] ($|y_{\text{CMS}}| < 0.9$ [9]) for D^0 (J/ψ) in pp and $-0.96 < y_{\text{CMS}} < 0.04$ [8] ($-1.37 < y_{\text{CMS}} < 0.43$ [10]) for D^0 (J/ψ) in p–Pb. Note also that the results for D^0 and J/ψ in p–Pb collisions are for the 0–100% multiplicity class.

1144 Furthermore, for the light-flavour hadrons, the mean transverse momenta in p–Pb col-
1145 lisions are observed to be consistently higher than those in pp collisions at 7 TeV. The
1146 situation for the charm hadrons is different, where $\langle p_T \rangle$ appears compatible between both
1147 colliding systems. The discrepancy is likely due to different production mechanisms for
1148 heavy and light flavours and to a harder fragmentation of charm quarks. Specifically, the
1149 fact that $\langle p_T \rangle$ remains similar in pp and in p–Pb is consistent with an $R_{p\text{Pb}}$ ratio com-
1150 patible with unity at all p_T [8] for D^0 , and/or with the effects of shadowing in p–Pb which
1151 reduces the production at low p_T and thus increasing the overall $\langle p_T \rangle$ for J/ψ [10]; the
1152 small p_T hardening expected in pp when going from 5.02 to 7TeV is apparently not enough
1153 to counter-balance the situation.

1154 Because of small decrease of the $\langle p_T \rangle$ for proton and Λ relative to those for K^{*0} and
1155 ϕ , two different trends for mesons and baryons have been suggested [43]. Even including
1156 D^0 and J/ψ , as shown in Figure 48, a different trend for mesons and baryons cannot be
1157 convincingly established.

1158 **6.2 Particle yield ratios**

1159 **6.2.1 Integrated yield ratios of excited to ground-state hadrons**

1160 The integrated yield ratios of excited to ground-state hyperons [44, 4, 7, 6] with the same
1161 strangeness content, for different collision systems and energies, are shown in Figure 49
1162 as a function of system size. The ratio of $\Xi(1530)^0$ to Ξ is flat across the system and
1163 it complements the information derived from other resonance measurement for different
1164 lifetime which are shown in Figure 50.

1165 The short-lived resonances(ρ , K^* and Λ^*) which exhibit suppression from peripheral to
1166 central lead-lead collisions and with respect to thermal model in central lead-lead collisions.
1167 Currently favored explanation of is dominance of elastic re-scattering of decay daughters
1168 over regeneration in the hadronic phase.

1169 The constant behavior of the yield ratios of excited to ground-state hyperons with same
1170 strangeness content ($\Xi(1530)^0$ and Φ) indicates that neither regeneration nor re-scattering
1171 dominates with increasing collision system size because of its longer-lifetime.

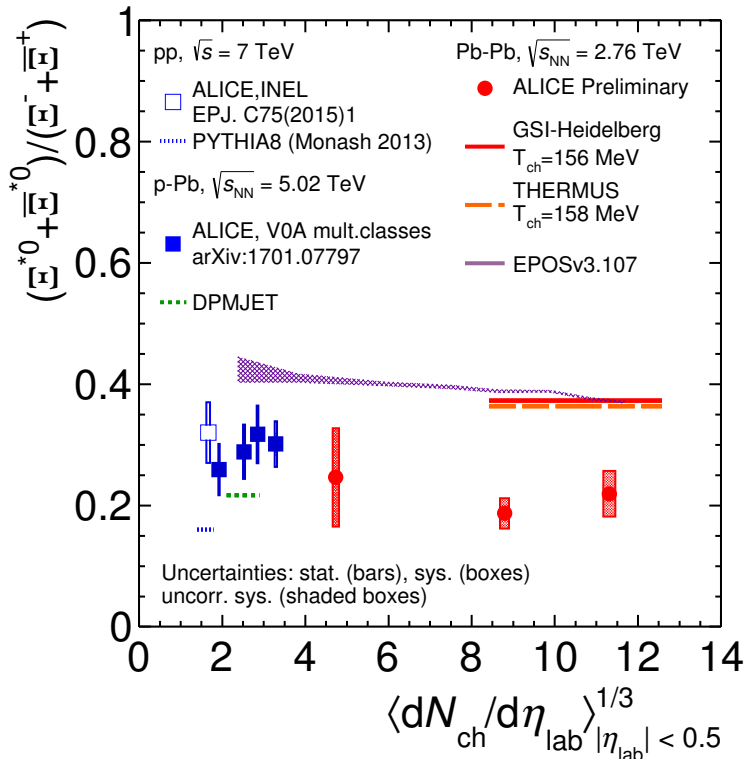


Figure 49: Ratio of $\Xi(1530)^0$ to Ξ^- measured in pp [7], p–Pb [4, 6] and Pb–Pb collisions as a function of $\langle dN_{ch}/d\eta_{lab} \rangle$ measured at midrapidity. Statistical uncertainties (bars) are shown as well as total systematic uncertainties (hollow boxes) and systematic uncertainties uncorrelated across multiplicity (shaded boxes). A few model predictions are also shown as lines at their appropriate abscissa.

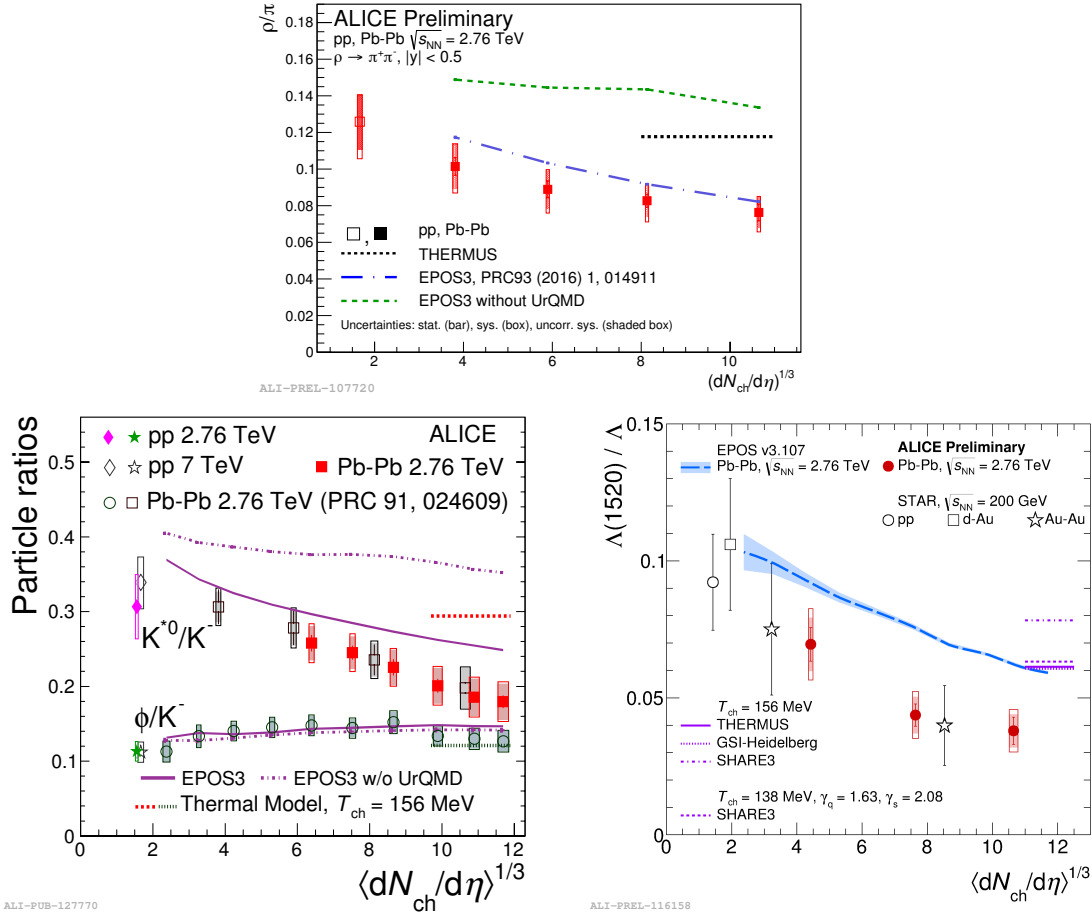


Figure 50: Ratio of ρ/π (Up), K^*/K , ϕ/K (Left bottom) and Λ^*/Λ with system size measured at mid-rapidity. Statistical uncertainties (bars) are shown as well as total systematic uncertainties (hollow boxes) and systematic uncertainties uncorrelated across multiplicity (shaded boxes). A few model predictions are also shown as lines at their appropriate abscissa.

1172 **6.3 Integrated yield ratios to pion**

1173 The integrated yield ratios of excited hyperons to pions are shown in Figure 51 to study
1174 the evolution of relative strangeness production yields with increasing collision system
1175 size. The ratio of $\Xi(1530)^0$ to Ξ is observed to be increase from pp to p–Pb collisions
1176 system and then, decrease from peripheral to central Pb–Pb collision. The QCD-inspired
1177 predictions like PYTHIA for pp [45] and DPMJET for p–Pb [37] clearly underestimate
1178 the observed yield ratios, while the statistical one seems to be comparable with results
1179 from high multiplicity in p–Pb but the ratio in Pb–Pb is below with respect to the model.
1180 The results in pp and p–Pb collisions are consistent with previous observation of ground-
1181 state hyperons to pion ratios. The Figure 52 presents particle yield ratios to pions of
1182 strange and multi-strange hadrons normalized to the values measured in pp collisions. As
1183 shown in the Figure 52, the $\Xi(1530)^0$ to pion ratios follow the trend of Ξ π as function of
1184 $\langle dN_{ch}/d\eta_{lab} \rangle$ and indicate that the strangeness enhancement observed in p–Pb collisions
1185 depends predominantly on the strangeness content, rather than on the hyperon mass.

1186 The Figure 53 also shows the hyperon-to-pion ratios and compared with model predic-
1187 tions. The

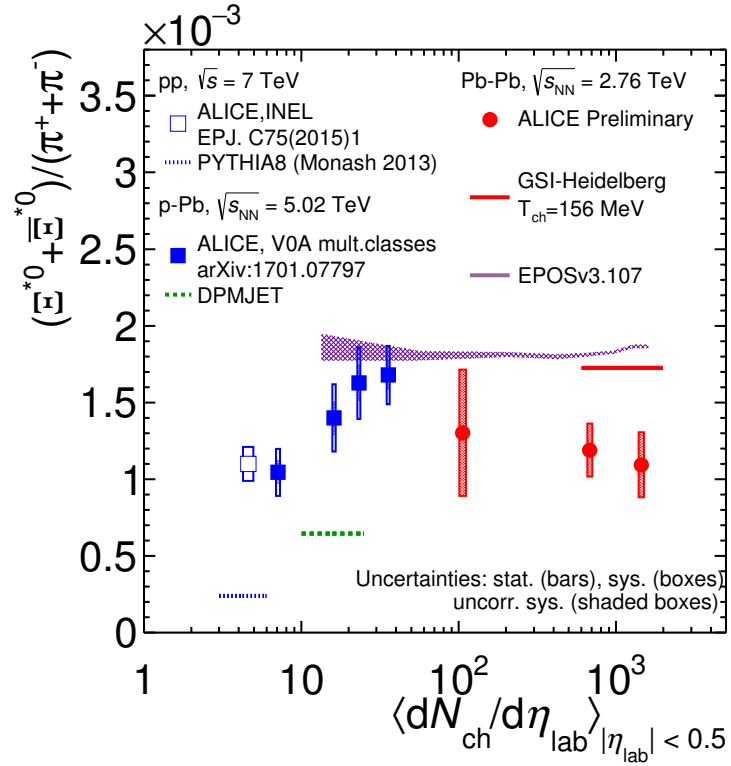


Figure 51: Ratio of $\Xi(1530)^0$ to π^\pm , measured in pp [11] and p-Pb [7] collisions, as a function of the average charged particle density ($\langle dN_{ch}/d\eta_{lab} \rangle$) measured at mid-rapidity. Statistical uncertainties (bars) are shown as well as total systematic uncertainties (hollow boxes) and systematic uncertainties uncorrelated across multiplicity (shaded boxes). A few model predictions are also shown as lines at their appropriate abscissa.

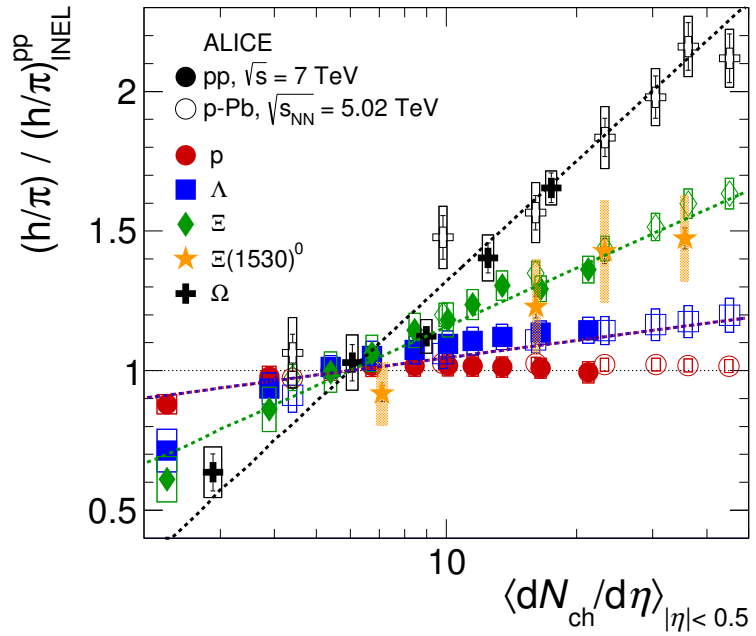


Figure 52: Particle yield ratios to pions of strange and multi-strange hadrons normalized to the values measured in pp collisions, both in pp and in p-Pb collisions. The common systematic uncertainties cancel in the double-ratio. The empty boxes represent the remaining uncorrelated uncertainties. The lines represent a simultaneous fit of the results with the empirical scaling formula in Equation ??.

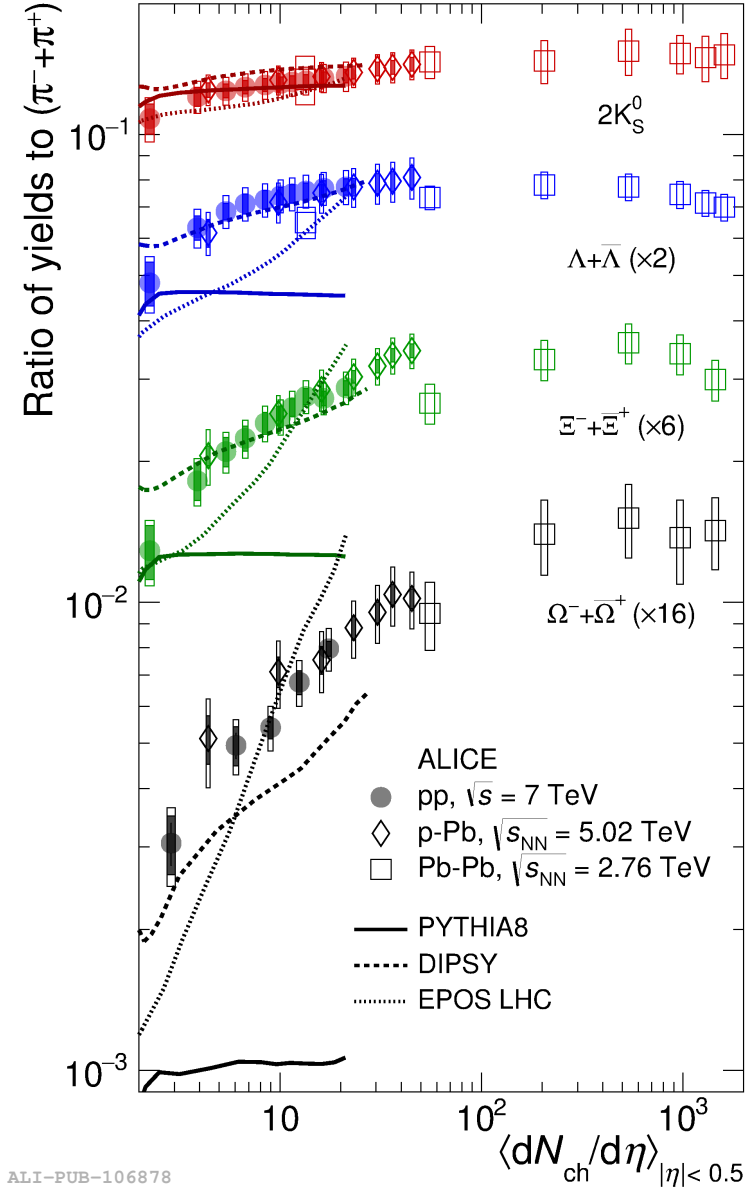


Figure 53: p_T -integrated yield ratios of strange and multi-strange hadrons to $(\pi^+ + \pi^-)$ as a function of $\langle dN_{ch}/d\eta_{lab} \rangle$ measured in the rapidity interval $|\eta| < 0.5$. The empty and dark-shaded boxes show the total systematic uncertainty and the contribution uncorrelated across multiplicity bins, respectively. The values are compared to calculations from MC models and to results obtained in Pb–Pb and p–Pb collisions at the LHC.

1188 **References**

- 1189 [1] **Particle Data Group** Collaboration, K. Olive *et al.*, “Review of Particle Physics,”
1190 *Chin. Phys. C* **38** (2014) 090001.
- 1191 [2]
- 1192 [3] **ALICE** Collaboration, K. e. a. Aamodt, “Alignment of the ALICE Inner Tracking
1193 System with cosmic-ray tracks,” *JINST* **5** (2010) P03003.
- 1194 [4] **ALICE** Collaboration, J. Adam *et al.*, “Multiplicity dependence of pion, kaon,
1195 proton and lambda production in p–Pb collisions at $\sqrt{s_{\text{NN}}}= 5.02$ TeV,” *Phys. Lett.*
1196 **B728** (2014) 25–38, [arXiv:1307.6796](https://arxiv.org/abs/1307.6796) [nucl-ex].
- 1197 [5] **ALICE** Collaboration, J. Adam *et al.*, “Production of $K^*(892)^0$ and $\phi(1020)$ in
1198 p–Pb collisions at $\sqrt{s_{\text{NN}}}= 5.02$ TeV,” *Eur. Phys. J. C* **76** (2016) 245,
1199 [arXiv:1601.7868](https://arxiv.org/abs/1601.7868) [nucl-ex].
- 1200 [6] **ALICE** Collaboration, J. Adam *et al.*, “Multi-strange baryon production in p–Pb
1201 collisions at $\sqrt{s_{\text{NN}}}= 5.02$ TeV,” *Phys. Lett. B* **758** (2016) 389–401,
1202 [arXiv:1512.07227](https://arxiv.org/abs/1512.07227) [nucl-ex].
- 1203 [7] **ALICE** Collaboration, B. Abelev *et al.*, “Production of $\Sigma(1385)^{\pm}$ and $\Xi(1530)^0$ in
1204 proton-proton collisions at $\sqrt{s}= 7$ TeV,” *Eur. Phys. J. C* **75** (2015) 1,
1205 [arXiv:1406.3206](https://arxiv.org/abs/1406.3206) [nucl-ex].
- 1206 [8] **ALICE** Collaboration, J. Adam *et al.*, “ D -meson production in p–Pb collisions at
1207 $\sqrt{s_{\text{NN}}}= 5.02$ TeV and in pp collisions at $\sqrt{s}= 7$ TeV,” *Phys. Rev. C* **94** (2016)
1208 054908, [arXiv:1605.07569](https://arxiv.org/abs/1605.07569) [nucl-ex].
- 1209 [9] **ALICE** Collaboration, B. Abelev *et al.*, “Inclusive J/ψ production in pp collisions
1210 at $\sqrt{s}= 2.76$ TeV,” *Phys. Lett. B* **718** (2012) 295–306, [arXiv:1203.3641](https://arxiv.org/abs/1203.3641) [hep-ex].
- 1211 [10] **ALICE** Collaboration, J. Adam *et al.*, “Rapidity and transverse-momentum
1212 dependence of the inclusive J/ψ nuclear modification factor in p–Pb collisions at
1213 $\sqrt{s_{\text{NN}}}= 5.02$ TeV,” *JHEP* **06** (2015) 55, [arXiv:1503.07179](https://arxiv.org/abs/1503.07179) [nucl-ex].
- 1214 [11] **ALICE** Collaboration, J. Adam *et al.*, “Measurement of pion, kaon and proton
1215 production in proton-proton collisions at $\sqrt{s}= 7$ TeV,” *Eur. Phys. J. C* **75** (2015)
1216 226, [arXiv:1504.00024](https://arxiv.org/abs/1504.00024) [nucl-ex].
- 1217 [12] F. Halzen and A. Martin.
- 1218 [13] S. Wheaton, J. Cleymans, and M. Hauer, “THERMUS: A Thermal model package
1219 for ROOT,” *Comput. Phys. Commun.* **180** (2009) 84–106, [hep-ph/0407174](https://arxiv.org/abs/hep-ph/0407174).

- 1220 [14] J. Cleymans, S. Kabana, I. Kraus, H. Oeschler, K. Redlich, and N. Sharma,
 1221 “Antimatter production in proton-proton and heavy-ion collisions at ultrarelativistic
 1222 energies,” *Phys. Rev.* **C84** (2011) 054916, [arXiv:1105.3719](https://arxiv.org/abs/1105.3719) [hep-ph].
- 1223 [15] L. Evans and P. Bryant.
- 1224 [16]
- 1225 [17]
- 1226 [18]
- 1227 [19]
- 1228 [20]
- 1229 [21]
- 1230 [22] **ALICE** Collaboration, K. Aamodt *et al.*, “The ALICE experiment at the CERN
 1231 LHC,” *JINST* **3** (2008) S08002.
- 1232 [23] **ALICE** Collaboration, L. B. et al, “Definition of the ALICE coordinate system and
 1233 basic rules for sub-detector components numbering,” *In Internal Note
 1234 ALICE-INT-2003-038* .
- 1235 [24] **ALICE** Collaboration, J. e. a. Alme, “The ALICE TPC, a large 3-dimensional
 1236 tracking device with fast readout for ultra-high multiplicity events,” *In Nuclear
 1237 Instruments and Method in Physics Research* **A622** (2010) 316–367.
- 1238 [25]
- 1239 [26] R. Glauber.
- 1240 [27] A. S. K.C. Chung, C.S. Whang and G. Pech.
- 1241 [28] **ALICE** Collaboration, J. Adam *et al.*, “Centrality dependence of particle
 1242 production in p–Pb collisions at $\sqrt{s_{\text{NN}}}= 5.02$ TeV,” *Phys. Rev.* **C91** (2015) 064905,
 1243 [arXiv:1412.6828](https://arxiv.org/abs/1412.6828) [nucl-ex].
- 1244 [29] **ALICE** Collaboration, B. Abelev *et al.*, “Centrality determination of Pb–Pb
 1245 collisions at $\sqrt{s_{\text{NN}}}= 2.76$ TeV with ALICE,” *Phys. Rev.* **C88** (2013) ,
 1246 [arXiv:1303.0737](https://arxiv.org/abs/1303.0737) [nucl-ex].
- 1247 [30]
- 1248 [31]

- 1249 [32] e. a. Bagnasco. S.
- 1250 [33] R. Brun and F. Rademakers.
- 1251 [34] **ALICE** Collaboration, B. Abelev *et al.*, “Performance of the ALICE Experiment at
1252 the CERN LHC,” *Int. J. Mod. Phys. A***29** (2014) 1430044, [arXiv:1402.4476](https://arxiv.org/abs/1402.4476)
1253 [nucl-ex].
- 1254 [35] **ALICE** Collaboration, B. Abelev *et al.*, “Pseudorapidity Density of Charged
1255 Particles in p–Pb Collisions at $\sqrt{s_{\text{NN}}}=5.02$ TeV,” *Phys. Rev. Lett.* **110** (2013)
1256 032301, [arXiv:1210.3615](https://arxiv.org/abs/1210.3615) [nucl-ex].
- 1257 [36] **ALICE** Collaboration, K. Aamodt *et al.*, “Strange particle production in
1258 proton-proton collisions at $\sqrt{s}=0.9$ TeV with ALICE at the LHC,” *Eur. Phys. J.*
1259 **C71** (2011) 1594, [arXiv:1012.3257](https://arxiv.org/abs/1012.3257) [nucl-ex].
- 1260 [37] S. Roesler, R. Engel, , and J. Ranft, “The Monte Carlo Event Generator
1261 DPMJET-III, Advanced Monte Carlo for Radiation Physics, Particle Transport
1262 Simulation and Applications,” *Conference Proceedings, MC2000, Lisbon, Portugal,*
1263 *October 23–26* (2000) 1033–1038, [hep-ph/0012252](https://arxiv.org/abs/hep-ph/0012252).
- 1264 [38] R. Brun, F. Carminati, and S. Giani, “GEANT detector description and simulation
1265 tool,” *CERN-W5013* (1994) .
- 1266 [39] R. Barlow, “Systematic Errors: Facts and Fictions,” *Presented at Advanced
1267 Statistical Techniques in HEP, Durham, March 2002* (2002) 333p,
1268 [hep-ex/0207026v1](https://arxiv.org/abs/hep-ex/0207026v1).
- 1269 [40] **ALICE** Collaboration, B. Abelev *et al.*, “Multi-strange baryon production at
1270 mid-rapidity in Pb–Pb collisions at $\sqrt{s_{\text{NN}}}=2.76$ TeV,” *Phys. Lett. B***728** (2014)
1271 216–227, [arXiv:1307.5543](https://arxiv.org/abs/1307.5543) [nucl-ex].
- 1272 [41] **ALICE** Collaboration, B. Abelev *et al.*, “Centrality dependence of π , K and p
1273 production in Pb–Pb collisions at $\sqrt{s_{\text{NN}}}=2.76$ TeV,” *Phys. Rev. C***88** (2013) ,
1274 [arXiv:1301.4361](https://arxiv.org/abs/1301.4361) [nucl-ex].
- 1275 [42] **STAR** Collaboration, B. I. Abelev *et al.*, “Hadronic resonance production in d–Au
1276 collisions at $\sqrt{s_{\text{NN}}}=200$ GeV measured at the BNL Relativistic Heavy-Ion Collider,”
1277 *Phys. Rev. C***78** (2008) 044906, [arXiv:0801.0450](https://arxiv.org/abs/0801.0450) [nucl-ex].
- 1278 [43] A. Velásquez, “Mean p_{T} scaling with m/n_q at the LHC: Absence of (hydro) flow in
1279 small systems?,” *Nucl. Phys. A***943** (2015) 9–17, [arXiv:1506.00584](https://arxiv.org/abs/1506.00584) [hep-ph].
- 1280 [44] **ALICE** Collaboration, B. Abelev *et al.*, “Multi-strange baryon production in pp
1281 collisions at $\sqrt{s}=7$ TeV with ALICE,” *Phys. Lett. B***712** (2012) 309,
1282 [arXiv:1204.0282](https://arxiv.org/abs/1204.0282) [nucl-ex].

- 1283 [45] T. Sjöstrand, S. Mrenna, and P. Skands, “A brief introduction to PYTHIA 8.1,”
1284 *Comput. Phys. Comm.* **178** (2008) 852–867, [arXiv:0710.3820 \[hep-ph\]](https://arxiv.org/abs/0710.3820).

1285 **Acknowledgements**